Total Hadronic Photoabsorption Cross Sections on Hydrogen and Complex Nuclei from 4 to 18 GeV*

D. O. Caldwell,† V. B. Elings, W. P. Hesse, R. J. Morrison, and F. V. Murphy
Department of Physics, University of California, Santa Barbara, California 93106

and

D. E. Yount‡
Stanford Linear Accelerator Center, Stanford University, Stanford, California 94305
(Received 18 September 1972)

Final total cross sections are given for a counter experiment at SLAC on hadronic photon absorption in hydrogen, deuterium, carbon, copper, and lead at incident energies from 3.7 to 18.3 GeV. Some of the nucleon cross sections have been revised and the C, Cu, and Pb data from 3.7 to 7.4 GeV have not been reported previously. The cross sections for complex nuclei vary approximately as $A^{0.9}$ in our energy range, indicating that the photon interacts, at least partially, as a strongly interacting particle. The energy dependences of the proton and neutron cross sections are also similar to those of hadron-nucleon cross sections and hence may be fitted by a typical Regge parametrization, yielding $\sigma_T(\gamma p) = (98.7 \pm 3.6) + (65.0 \pm 10.1)\nu^{-1/2}$ μb and $\sigma_T(\gamma n) = (103.4 \pm 6.7) + (33.1 \pm 19.4)\nu^{-1/2}$ μb, where ν is the photon energy in GeV. These extrapolate to the same value at infinite energy, consistent with Pomeranchukon exchange, and the energy-dependent part yields an isovector-to-isoscalar-exchange ratio of 0.18 ± 0.06. While these observations are qualitatively consistent with vector meson dominance, quantitatively *vector dominance fails* in relating our results to ρ photoproduction on hydrogen or to experiments determining the ρ-nucleon cross section. Vector dominance cannot be rescued by assuming that the ρ-photon coupling constant depends on the photon mass. Instead, *an additional short-range interaction is apparently required,* possibly due to a heavy ($\gtrsim 2$ GeV/c^2) vector meson or to a bare-photon interaction. The additional interaction accounts for approximately 20% of the total photoabsorption cross section.

I. INTRODUCTION

The complete results of an experiment on photoabsorption by hydrogen, deuterium, carbon, copper, and lead for the energy range from 3.7 to 18.3 GeV are presented. Portions of the data, reported earlier,[1,2] have shown that the photon exhibits a hadronlike behavior. In particular, the dependence of the photon-nuclear cross section on the nucleon number A established the fact that higher-energy photons are shadowed by nucleons in the nucleus.[1] Further evidence for hadronlike behavior of the photon is the near equality of the neutron and proton cross sections and the observation that the energy dependence of these cross sections is very similar to that of pion-nucleon total cross sections. In this paper we present all of the data from the experiment and give a detailed comparison with the vector-meson-dominance (VMD) model, which is normally invoked to explain this hadronlike behavior of photon cross sections. We find that the vector-meson-dominance model does *not* agree quantitatively with the data, and that the results suggest that a short-range photon-nucleon interaction contributes significantly to the total cross section.

At high energy the dominant photoabsorption reactions are the production of the vector mesons ρ, ω, and ϕ. These processes are predominantly diffractive, like the elastic scattering of hadrons on the nucleon. In particular, the total cross sections for these reactions are nearly constant in energy, and the differential cross sections show a forward peak with a slope which is similar to that of pion-nucleon scattering. To explain this behavior[3] the vector-meson-dominance model,[4] in which the photon dissociates into a hadron state with the same quantum numbers as the photon, has been developed. These states are assumed to be the known vector mesons, the ρ, ω, and ϕ. The photon interacts, as shown in Fig. 1(a), by first becoming a vector meson, V [with coupling $(\pi\alpha)^{1/2}/\gamma_V$], which then scatters from the nucleon with a cross section typical of hadron-hadron scattering. The ρ production amplitude $f(\gamma p \to \rho p)$, for example, is then related to the ρ scattering amplitude $f(\rho p \to \rho p)$:

$$f(\gamma p \to \rho p) = \frac{(\pi\alpha)^{1/2}}{\gamma_\rho} f(\rho p \to \rho p). \quad (1)$$

Given measured values for the couplings and the

forward scattering amplitudes of the known vector mesons, the model gives a simple prediction for forward Compton scattering,

$$f(\gamma p \to \gamma p)|_{t=0} = \sum_V \frac{\pi\alpha}{\gamma_V^2} f(Vp \to Vp)|_{t=0}, \tag{2}$$

as indicated in Fig. 1(b).

Using the optical theorem,[5]

$$\sigma_T(AB) = \frac{4\pi}{k} \mathrm{Im} f(AB \to AB)|_{t=0}, \tag{3}$$

we can relate the photon total cross section to the vector meson scattering amplitudes,

$$\sigma_T(\gamma p) = \frac{\pi}{k} \sum_V \frac{4\pi\alpha}{\gamma_V^2} \mathrm{Im} f(Vp \to Vp)|_{t=0}, \tag{4}$$

and, using Eq. (1), to the photoproduction amplitudes,

$$\sigma_T(\gamma p) = \frac{\pi}{k} \sum_V \frac{4\pi\alpha}{\gamma_V^2} \frac{\gamma_V}{(\pi\alpha)^{1/2}} \mathrm{Im} f(\gamma p \to Vp)|_{t=0}. \tag{5}$$

The forward amplitude is related to the differential cross section,

$$|f_{t=0}|^2 = (1+\eta_V^2)(\mathrm{Im} f_{t=0})^2 = \frac{k^2}{\pi} \left.\frac{d\sigma}{dt}\right|_{t=0}, \tag{6}$$

where η_V is the ratio of real to imaginary parts, so that the total cross section can be predicted in terms of other measurable quantities:

$$\sigma_T(\gamma p) = \sum_{\rho,\omega,\phi} \left(4\pi \frac{4\pi\alpha}{\gamma_V^2} \frac{1}{1+\eta_V^2} \left.\frac{d\sigma}{dt}(\gamma p \to Vp)\right|_{t=0} \right)^{1/2}. \tag{7}$$

The crucial question for the vector-meson-dominance model is whether the measured total cross section agrees with the right-hand side of Eq. (7).

Photoabsorption cross sections measured on complex nuclei provide a further test for VMD, particularly probing the range of the interactions. For hadrons, which have mean free paths in nuclei short compared to the nuclear size, nuclei act like absorbing disks whose total cross sections tend to increase with A as the nuclear area, or roughly $A^{2/3}$. However, since photons have absorption cross sections about 200 times smaller than those of hadrons, their long mean free paths would imply nuclear cross sections proportional to A. This intuitive view, that all nucleons would be equally likely to interact and that none would "shadow" any other is then diametrically opposed to the argument, which has long been known,[6] that the photon would interact as a hadron by becoming a vector meson, as VMD would predict.

The photon-nuclear interaction via vector mesons can be viewed as an interference between two processes shown in Fig. 1(c), which give the total Compton amplitude and thus $\sigma_T(\gamma A)$. The one-step amplitude, for which the scattering takes place on a single nucleon, occurs equally well at the nuclear surface or inside nuclear matter. The two-step amplitude, in which a vector meson is produced on one nucleon and in a subsequent scattering couples back to the photon, occurs only inside the nucleus. The two amplitudes tend to interfere destructively, and in VMD at infinite energy the destructive interference is perfect inside nuclear matter, leaving only a surface interaction. However, at finite energies the vector meson (because of its mass) has less momentum,

$$k_V = (k_\gamma^2 - m_V^2)^{1/2} \approx k_\gamma - \frac{m_V^2}{2k_\gamma}, \tag{8}$$

with a correspondingly larger wavelength so that the two waves lose phase coherence over a typical distance, $R \sim 2k_\gamma/m_V^2$.[7] At high energy, such that the range R is not only larger than the nuclear size, but also much larger than the vector-meson-interaction mean free path, each nucleon should shadow those behind it. Under these conditions, the interacting nucleons lie predominantly on the nuclear surface, and the total nuclear photoabsorption cross section, $\sigma_T(\gamma A)$, will increase with nuclear size less rapidly than the number of nucleons, A.

It is convenient to work with the *effective number of nucleons* in the target,

$$A_{\mathrm{eff}} = \frac{\sigma_T(\gamma A)}{\sigma_T(\gamma N)}. \tag{9}$$

For each target and energy one divides the cross

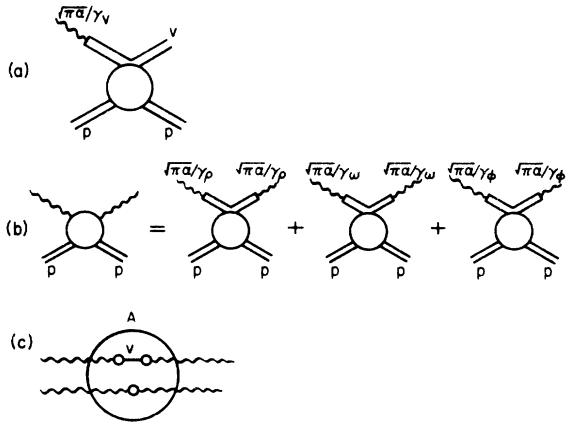

FIG. 1. (a) Photon interaction with a nucleon through a vector meson. (b) Compton scattering pictured as the sum of interactions of the three known vector mesons coupled to the photon. (c) The one-step and two-step processes which can occur for a photon interacting in a nucleus.

section by the average nucleon cross section appropriate to that target and energy,

$$\sigma_T(\gamma N) = \frac{Z}{A}\sigma_T(\gamma p) + \left(1 - \frac{Z}{A}\right)\sigma_T(\gamma n), \tag{10}$$

where $\sigma_T(\gamma p)$ and $\sigma_T(\gamma n)$ are determined experimentally. This procedure removes the small energy dependence of the nucleon cross sections from the quantity A_{eff}. In addition, A_{eff} is independent of the values of the coupling constants to lowest order. Clearly, if the interaction were completely short-range, then all of the nucleons would be equally likely to interact with a photon, giving $A_{\text{eff}} = A$. On the other hand, if the interaction were entirely long-range and the vector-meson-interaction mean free paths very short, then only the surface nucleons would contribute, giving $A_{\text{eff}} = A^{2/3}$.

The actual vector-dominance predictions for A_{eff} lie between these two extremes and are obtained from a rather sophisticated optical model,[8] which includes the use of a two-nucleon correlation length l_c, as well as energy-dependent η_ρ and

$$\sigma_T(\rho N) = \sigma_T(\rho p)[\sigma_T(\gamma N)/\sigma_T(\gamma p)],$$

where

$$\sigma_T(\rho p) = \tfrac{1}{2}[\sigma_T(\pi^+ p) + \sigma_T(\pi^- p)]$$

from the quark model. The values of $\sigma_T(\rho p)$ change by 12% from 4 to 16 GeV and agree with determinations from ρ photoproduction.

The data reported here for photon absorption on hydrogen from 3.7 to 18.3 GeV are used to test the VMD predictions of Eq. (7). In addition, utilizing data on deuterium, a Regge parametrization of the neutron and proton cross section is given. Data for photoabsorption on complex nuclei are presented for the same energy region and compared with the second VMD prediction, the A dependence of the nuclear cross section. The results of the two types of comparison indicate that in addition to a VMD type of interaction, the photon has a significant interaction of short-range character.

II. EXPERIMENTAL APPARATUS

A. Preliminary Considerations

At the time this experiment was proposed (April, 1968), it was generally believed to be exceedingly interesting and also exceedingly difficult, particularly at SLAC where the energy is high, but where the duty cycle is 2 orders of magnitude lower than for electron synchrotrons. The fundamental problem in measuring these cross sections arises from electromagnetic interactions in the target, which in our case are 90 to 2600 times more numerous than the hadronic events, depending upon the target material.

To measure photoabsorption total cross sections, it is necessary to determine (a) the number of photons incident with a given energy and (b) the fraction of these photons that interact hadronically in a target of known thickness and material. The fraction interacting can be determined either by (1) detecting final-state hadrons or (2) observing the hadronic absorption and thus the absence of the photon or electromagnetic-interaction products in the final state. Finally, there are three crucial ideas, each separately well known, which together reduce the difficulties in this experiment to a remarkably low level. These are: (a) the use of a tagged-photon beam, (b) the fact that a shower detector has the same response to an electron-positron pair as to the photon that produced the pair, and (c) the fact that geometry alone suffices to separate hadronic and electromagnetic processes in a system with even rudimentary energy discrimination.

B. Outline of the Experiment

The experimental implementation of the above ideas is shown schematically in Fig. 2. A well-collimated, momentum-analyzed beam of positrons was incident from the left with negligible beam halo. Those positrons that emitted bremsstrahlung photons in a thin radiator were deflected by the tagging magnet into a tagging hodoscope, providing a one-to-one correspondence between the detected positrons and beam photons. Tagging (T) thus determined the number of photons incident and the energy of each photon, and it discriminated effectively against backgrounds that were not in coincidence with a particular tagged photon. The tagging efficiency, defined as the probability that a tagging signal in fact corresponded to a tagged photon of the proper energy, was significantly improved by using anticounters (A) at the appropriate locations.

Photons that did not interact, as well as the products of any electromagnetic interactions, remained very close to the original beam line ($\theta \sim m_e c^2/E_\gamma$) and passed easily through the beam hole in the hadron counters ($S2a$ and $S2b$), continuing downstream until they reached the shower counter ($S1$) directly in the beam line. The original photons and the products of electromagnetic interactions were detected with equal efficiency in a shower counter so that the energy observed in $S1$ balanced the energy tagged by T. Hadronic photon absorption was thus indicated by a tagging signal without a coincident pulse in either A or $S1$, $T\overline{AS1}$, which would have been sufficient to carry

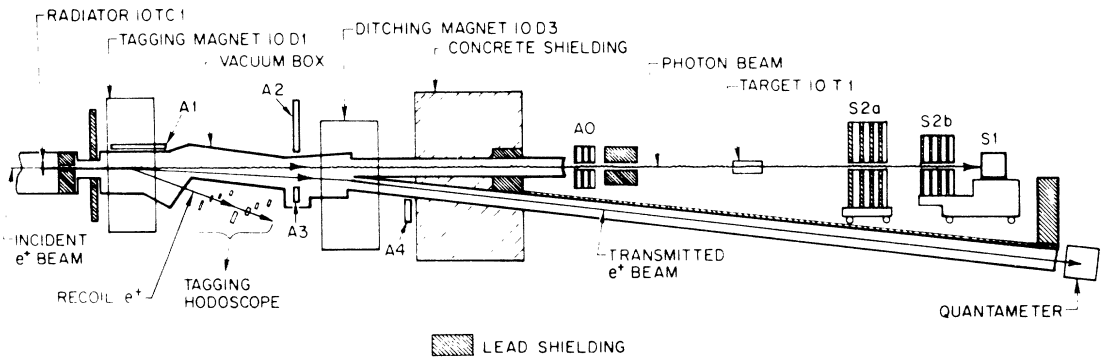

FIG. 2. Side view of the photon beam and experimental apparatus (not to scale).

out the experiment if the tagging inefficiency could have been reduced below some ten parts per million. The inefficiency, for this experiment, was in the range from 1.2% to 0.3%, due largely to the halo-free beam and the judicious use of the counters T, A, and $S1$.

Final-state hadrons were characterized by appreciable opening angles ($\theta \gtrsim m_\pi/E_\gamma$) and generally did not reach $S1$. Instead, they were detected by lead-scintillator sandwiches $S2a$ and $S2b$, which had sufficient energy resolution to exclude the low-energy products of electromagnetic interactions that sometimes did attain appreciable angles. Two hadron detectors permitted the inner and outer hadron-acceptance angles to be varied independently, thereby demonstrating experimentally that the rate was insensitive to these angular limits over some range, i.e., that the hadronic interactions were detected with good efficiency and that the electromagnetic backgrounds were small. Hadronic interactions were thus signaled by $T\bar{A}S2$, which would again have sufficed to carry out the experiment if the relevant backgrounds had been 1% or less of the hadronic rate.

In practice, the effectiveness of $T\bar{A}S2$ was similar to that of $T\overline{AS1}$, so that the redundant event signature $T\overline{AS1}S2$ provided the necessary background discrimination. The pulse heights obtained in $S1$ and $S2$ were recorded on magnetic tape for each of the three signatures mentioned, thus permitting further detailed analysis off-line.

C. Positron Beam

The beam-transport system is shown in Fig. 3. The primary electron beam from SLAC struck a positron converter, $TC61$, typically $0.05X_0$ thick. Positrons emerging from the converter were momentum-analyzed and separated from electrons and photons by $B61$ and focused by $Q60/Q61$ at the positron momentum-selection collimator. There were no collimators or air gaps intercepting the positron beam after this point. Additional bending by $9D3$ and $10D1$ swept out halo particles, recombined momenta, and brought the positrons to the bremsstrahlung radiator at $10TC1$. The quadrupoles $10Q1$ and $10Q2$ were adjusted to focus positrons, and thus tagged photons, at the target distance.

Secondary positrons were used in this experiment, rather than primary electrons, since the required intensity, about 5×10^3 positrons per pulse, was lower than the primary electron intensity by 7 decades. Positrons were also better for tagging, since atomic electrons ejected from the bremsstrahlung radiator could not simulate positrons that had radiated. Positron energies as high as 95% of the electron energy were used, and the full-width momentum spread was 0.75%. Beam profiles obtained at the bremsstrahlung radiator with a detector having a 0.32-cm diameter are shown in Fig. 4. The full width at half maximum was 0.59 cm horizontally and 0.29 cm vertically, and the beam halo outside a 1-cm-diameter envelope was remarkably low.

After passing through the radiator, the positrons were deflected in vacuum by the tagging magnet $10D1$ and ditching magnet $10D3$ into a quantameter.[9] The vacuum pipe was shielded on the left and on the right by concrete blocks and was shielded from the counters above by lead bricks having a total thickness normal to the pipe of 20 cm. The quantameter located downstream monitored the positron intensity and dissipated the beam energy. A double (horizontal and vertical) split-plate ion chamber[9] was mounted inside the vacuum tank just upstream of the radiator and could be lowered pre-

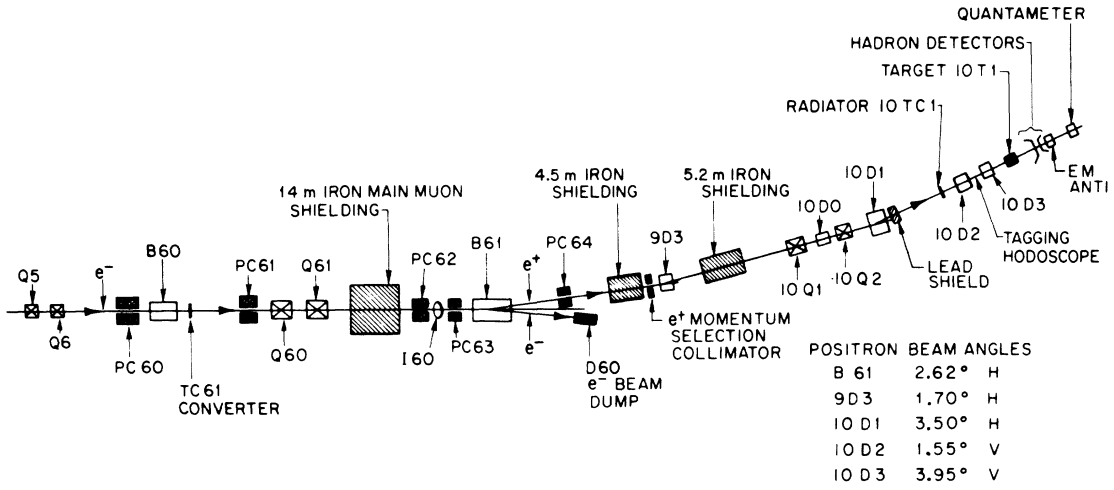

FIG. 3. Top view of the primary and secondary beam-transport systems (not to scale).

cisely into the beam line to center the positron beam at this location. A 2.5-cm-long, 1-cm-diameter lead plug was mounted on the front window of the ion chamber to increase its sensitivity.

D. Tagged-Photon Beam

The elements of the tagged-photon beam were shown previously in Fig. 2. The positron beam was first incident on a bremsstrahlung radiator at $10TC1$. The copper radiators were 1 cm in diameter and were suspended in vacuum by 1-mm-wide copper strips to minimize possible interactions by particles in the beam halo. Four positions could be selected: empty radiator, $0.0005X_0$, $0.002X_0$, and $0.01X_0$. The radiator thickness was chosen to minimize the ratio of false to true tagging signals. False tags were generated by trident production, bremsstrahlung followed by pair production in the radiator, multiple bremsstrahlung, and by low-energy positrons in the incident beam which were swept directly into the tagging counters. With our clean beam, it was advantageous to choose a thin radiator, $0.002X_0$, to minimize the multiple process events. This thickness yielded 4×10^{-4} tagged photons per positron, or about two tagged photons per beam pulse of 1.6 μsec duration.

The position of the photon beam at the $S2$ counters was determined with the aid of a 2.5-cm-long, 0.3-cm-diameter lead plug centered in a Lucite disk, temporarily mounted in the beam hole. A radiation monitor downstream allowed the photon beam to be detected when it interacted in the lead plug.

The photon intensity was monitored in four energy bins by four pairs of tagging counters. Each of these tagging channels had a positron energy acceptance of $0.05E_0$, and together they spanned the interval from $0.06E_0 < E_f < 0.26E_0$, where E_0 and E_f are, respectively, the incident and final positron energies. The corresponding photon energies are given by $E_\gamma = E_0 - E_f$ and thus lie in the range $0.74E_0 < E_\gamma < 0.94E_0$. Positron energy intervals and

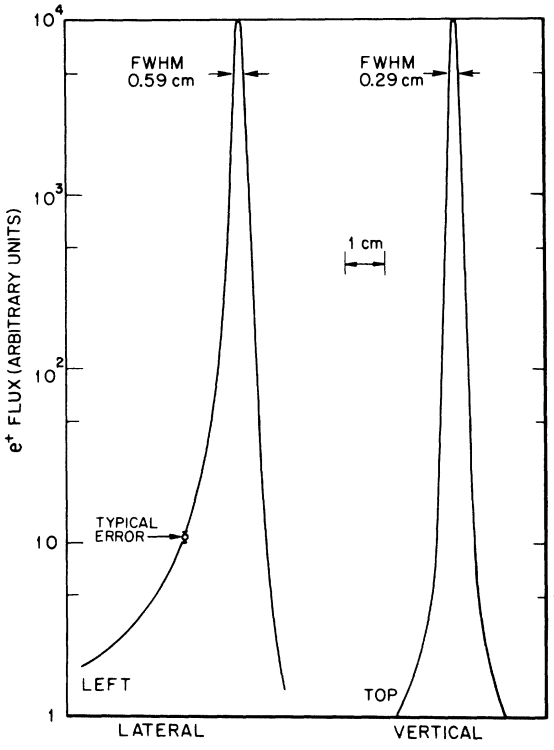

FIG. 4. Positron beam profiles at the photon radiator for a beam of 14-GeV positrons focused at the radiator.

tagging-counter locations were determined by floating a wire through the tagging magnet $10D1$. The two tagging counters in a given channel were spaced approximately 1 m apart along the positron trajectories to reduce the possibility of an accidental tag. The exit window of the vacuum chamber was made as thin as possible (0.16 cm aluminum) to minimize multiple scattering and radiation before tagging.

Photons produced in the radiator traveled forward 8.5 m in vacuum before exiting through a 0.25-mm Mylar window just upstream of the anticounter $A0$. The function of this shower detector, a three-layer, lead-scintillator sandwich with a 6-cm center hole, was to veto tags in which an energetic photon was outside the nominal beam envelope. $A0$ normally intercepted about 1.6% of the tagged photons when the incident positrons were at 4 GeV and about 0.1% when they were at 18 GeV. $A0$ was prevented from vetoing events originating in the target by a lead back-scatter shield 25 cm thick.

Anticounters $A1$ and $A2$ were used to veto electrons from trident or pair production in the radiator, thereby preventing the resulting low-energy positron from causing a spurious tag. Their effectiveness was enhanced by installing $A1$ within 10 cm of the beam line and by making the top windows of the vacuum chamber as thin as possible, in this case, 3 mm aluminum. Electrons were vetoed from 5 MeV up to 4 GeV when $10D2$ was set for 4-GeV positrons and from 24 MeV up to 18 GeV when $10D2$ was set for 18-GeV positrons.

Since the thickness at which the trident and pair-production processes are comparable is about $0.003-0.004X_0$,[10] trident production dominated for our $0.002X_0$ radiator thickness. Detailed calculations[11] indicate that in our geometry, the rate from these processes was of the order 10%. This was reduced to 0.8% at 5 GeV and 0.2% at 19.5 GeV incident positron energy by the $A1$ and $A2$ counters. Low-energy positrons contaminating the incident beam contributed 0.4% and 0.1%, respectively, at these two energies, as determined with the radiator out. The false-tag rates were thus 1.2% at 5 GeV and 0.3% at 19.5 GeV, of which two-thirds was associated with trident and pair production and one-third with beam positrons degraded in energy. These rates are averages over four channels, and it is worth noting that the false-tag rate increased by more than a factor of 5 from Channel 4 ($0.21E_0$ to $0.26E_0$) to Channel 1 ($0.06E_0$ to $0.11E_0$), in agreement with calculations[11] of the trident process.

Anticounters $A3$ and $A4$ were used to veto recoil positrons associated with photons of intermediate energy, $0.74E_0 > A3 > 0.50E_0$ and $0.65E_0 > A4 > 0.35E_0$, as shown in Fig. 5. Such photons, more numerous than those that were tagged, could (a) produce hadronic events in accidental coincidence with false tags or (b) simulate surviving photons in the shower counter $S1$ in accidental coincidence with tagged photons that were absorbed hadronically, thereby vetoing good events. These effects depended upon the energy resolution of the shower counter and particularly upon the counting rates and pulse widths of the detectors involved. The counter $A3$ protruded into the vacuum box within a reentrant aluminum cylinder with 1.5-mm wall thickness. This arrangement allowed $A3$ to be positioned empirically as close to the positron beam as possible, but without intercepting positrons in Channel 4.

Because of the high singles rates in the A counters and the short duty cycle, the tagging rate T was reduced by approximately 40% by the various anticounters $\bar{A}$. While most of the accidentally vetoed photons were genuine, the rate for false tags was reduced by more than one decade by this means. The loss in tagging rate did not affect the experimental results because the properly tagged photons $T\bar{A}$, which were relatively free of backgrounds and accidentals, were used as the monitor rather than the raw rate T.

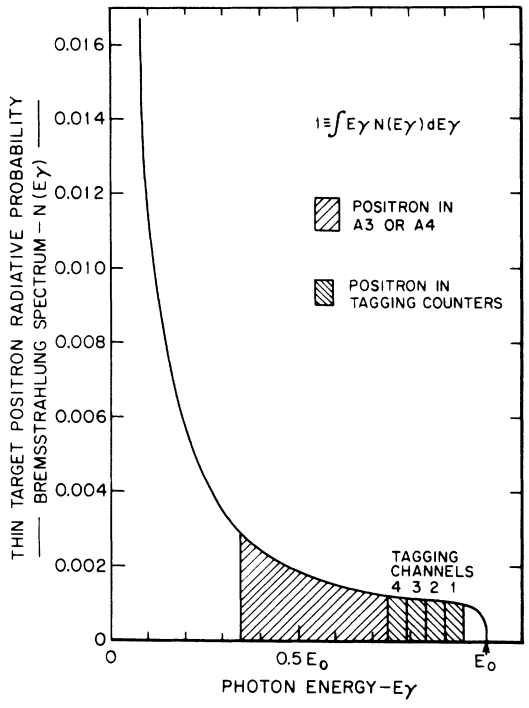

FIG. 5. Bremsstrahlung energy spectrum for a thin radiator. Photons in the interval $0.74E_0 < E_p < 0.94E_0$ were tagged for use in the experiment, while those in the interval $0.35E_0 < E_p < 0.74E_0$ were explicitly vetoed by the $A3$ and $A4$ counters.

E. Electromagnetic $S1$ and Hadronic $S2$ Detectors

Tagged photons that did not interact, as well as the products of electromagnetic interactions, were detected by a lead-scintillator shower counter $S1$ centered on the beam line. The 16 layers of lead were in the form of 24-cm-diameter disks 6 mm thick, sandwiched between 16 layers of plastic scintillator 25 cm×25 cm in area and also 6 mm thick. Light from each scintillator layer was conducted through an individual light pipe to a Lucite mixing block 45 cm above the counter. The combined output was viewed by a single 56-*DVP* phototube. The total thickness was $18.1X_0$, sufficient to contain 97% of the energy in a 20-GeV electromagnetic shower.[12] A positron-electron pair of a given total energy was detected by $S1$ with virtually the same pulse height as a single photon of the same energy. Since the more forward member of a pair carries most of the energy, in those rare cases in which one member of a pair originating in the event target was at a large enough angle to be counted as a hadron in $S2$, the more forward member still transmitted to $S1$ sufficient energy to define the interaction as electromagnetic. The probability that *both* members of a pair would be intercepted by $S2$, an occurrence which would be interpreted as a hadronic event, was negligible. The experimental energy resolution of $S1$ was approximately $\sigma_{S1} \approx 15\%/[E_\gamma\ (\mathrm{GeV})]^{1/2}$.

Under the conditions of this experiment, there was a large flux of electromagnetic particles at very small angles. At the larger angles, $\theta \gtrsim 400\ \mathrm{MeV}/E_0$, subtended by the hadron counters $S2a$ and $S2b$, the electromagnetic backgrounds were of low energy. As a consequence, these counters were designed to have a high efficiency for detecting hadrons, including π^0's, but a low efficiency for electromagnetic particles of energy below 1 GeV. This was accomplished by building both $S2a$ and $S2b$ as four-layer sandwiches of scintillator separated by 2.5 cm of lead. Each scintillator plane, 1 m×1 m for $S2a$ and 0.5 m×0.5 m for $S2b$, was viewed separately by a pair of photomultipliers. A hadronic interaction was then signaled by a fourfold coincidence in either $S2a$ or $S2b$ or by a summed pulse height from the two counters equivalent to three minimum-ionizing particles passing through four scintillation planes, corresponding roughly to a 1-GeV electromagnetic shower.

The detection efficiency for electrons of the $S2$ counters as used was known from tests carried out at the Stanford Mark III Accelerator at 225 MeV/c and 450 MeV/c and at SLAC at 2.3 GeV and 5.0 GeV. These results, which apply also to positrons and to photons to a good approximation, were interpolated with Monte Carlo predictions[12] to produce the efficiency-versus-momentum curve shown in Fig. 6. Data obtained with incident π^- at 0.75 GeV/c at the Berkeley Bevatron and at 2.3 GeV/c at SLAC are shown in the same figure. The 2.3-GeV/c point and that at 5.0 GeV/c (which does not appear in the figure) both give an efficiency of virtually 100%. Figure 6 indicates that the desired energy response for e^+, e^-, and γ had been achieved and that the efficiency for hadrons remained quite high even at energies below 1 GeV.

As shown in Fig. 2, $S2a$ and both $S2b$ and $S1$ were mounted on two carts which could be moved parallel to the beam, toward or away from the target. This made possible the optimization of the detection geometry with each value of the incident positron energy, and also facilitated important experimental checks. Data were taken with the $S2b$ and $S2a$ counters in various positions in order to establish that all hadronic events were being counted and that electromagnetic events were a negligible component of the signals. As the $S2b$ counter moved downstream, the inner acceptance angle decreased. It was observed that the signal was insensitive to the $S2b$ position until the angle subtended by the hole in $S2b$ was significantly less than $\theta^{\min} \sim 400\ \mathrm{MeV}/E_0$, the standard position (defined from the downstream end of the target). This was expected since at high energy nearly all of the final states include at least one particle with an angle larger than $\theta^{\min}$. The fraction of events in which both photons from a forward π^0 interact in $S1$ and have sufficient energy to veto the event was also very small. When the angle subtended by $S2b$

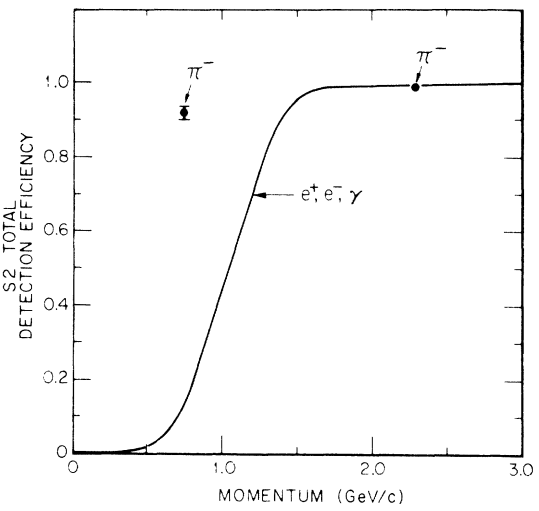

FIG. 6. Total $S2$ counter efficiency (fourfold and/or shower) measured for incident π^-, e^+, e^-. Monte Carlo electromagnetic-shower curves were used to calculate the efficiency for photons and to interpolate the efficiencies for e^+ and e^-.

was reduced further, both members of an electron pair were detected in *S2b* and the signal increased markedly.

Figure 7 illustrates the results of two of the geometry tests carried out with 4.84-GeV/c positrons and a deuterium target. The raw cross section σ_R, corrected only for deadtime, accidentals, empty target, and photon attenuation in the target, is plotted versus the relevant solid angles. As *S2b* moved downstream with *S2a* fixed, (a) there was a sharp increase in rate due to electromagnetic backgrounds. When *S2a* then moved downstream with S2b fixed, (b) there was a significant loss of hadrons. At this low, and consequently difficult energy, corrections for hadron loss and for electromagnetic backgrounds were necessary even with the two counters in the optimum geometry. Calculations of these corrections over broad angular ranges were consistent with test data of the types shown in Fig. 7.

F. Targets

The target flask and vacuum tank used with liquid hydrogen or liquid deuterium are shown schematically in Fig. 8. The flask was mounted in a long snout that cantilevered downstream of the main vacuum tank in order to minimize the material between the target and the event detectors. The flask was 101.50 ± 0.25 cm long at 20 °K and 10 cm in diameter. The entrance and exit windows of the flask were 0.14-mm Mylar, and the entrance and exit windows of the vacuum tank were, respectively, 0.25-mm Kapton and 0.15-mm aluminum. The empty-target rate calculated for hadronic interactions in the windows, the residual target gas, and the air drift spaces is 4.0×10^{-5} per incident photon, in good agreement with the observed rate of $(4.1\pm0.4)\times10^{-5}$. This is about 10% of the full-target rate for hydrogen and about 5% of the full-target rate for deuterium. The liquid temperatures were monitored continuously with the aid of two Rosemount Model 146*CP*-2 platinum resistors located, respectively, at the top of the flask near the vent line and at the bottom of the flask near the fill line. The target densities were determined from the mean temperature for each run using standard conversion tables.[13] Temperature variations during a typical run corresponded to density

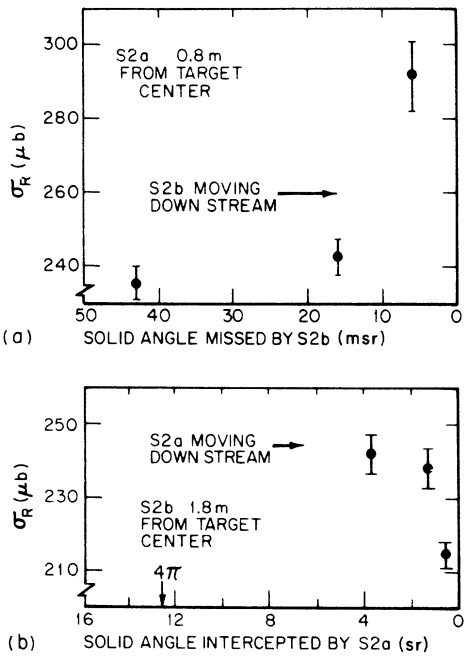

FIG. 7. Raw deuterium cross sections (corrected only for *S2* accidentals, deadtime in *S1*, photon attenuation in the target, and empty target) measured for various *S2a* and *S2b* positions. For *S2a* fixed upstream (a), the rate increased as *S2b* moved downstream indicating that electromagnetic backgrounds were beginning to be significant. For *S2b* fixed downstream (b), the rate decreased as *S2a* was moved downstream indicating that some wide-angle hadronic events were being lost.

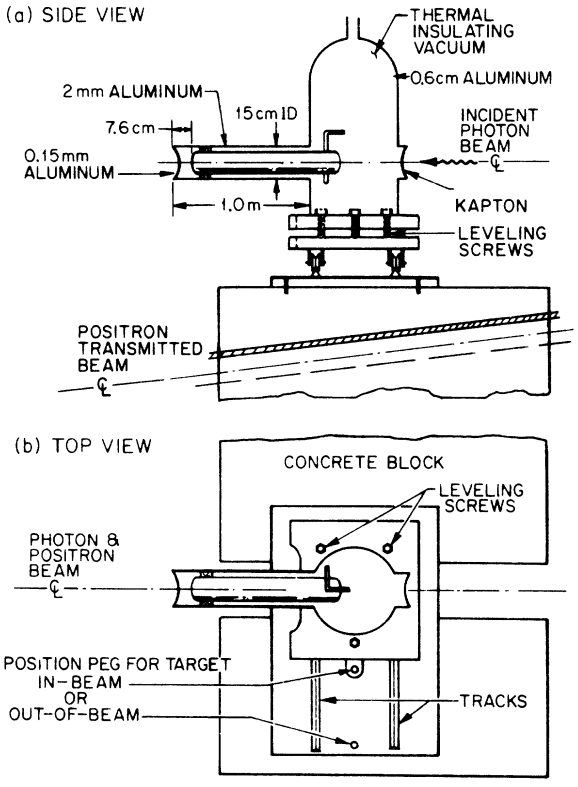

FIG. 8. Side view (a) and top view (b) of the liquid-target flask mounted in the insulating vacuum chamber. The flask was 101.50 ± 0.25 cm long at 20°K and 10 cm in diameter. The entrance and exit windows of the flask were 0.14-mm Mylar.

changes of less than 0.1%.

The solid targets were also mounted on the liquid-target support vehicle and were automatically centered in the beam line by rolling the liquid target to its out-of-beam position. A five-foot-long helium bag with 0.1-mm Mylar end windows was installed between the solid targets and the $A0$ counter to reduce the empty-target rate. The area of each solid target was approximately 10 cm×10 cm. Two blocks approximately 2.5 cm thick were used in the case of carbon, and two plates approximately 0.8 mm thick were used in the case of copper. The targets were homogeneous and the thicknesses uniform to better than ±0.1%. Target purities were known from both spectroscopic and chemical analysis. Impurities were negligible with one exception, namely, the lead target used with 16.2 GeV/c positrons (PbE), which contained 30% tin. Fortunately, this impurity can be taken into account by using the variation of rate with atomic number A determined in this experiment. Estimates of the empty-target rate for the solid-target configuration give 1.0×10^{-5} per incident photon, rather less than the $(2.8\pm0.6)\times10^{-5}$ observed experimentally. The anomalously high experimental rate is due apparently to the fact that nearly all of the spurious material is well upstream of the target location in this case so that electromagnetic backgrounds are significantly enhanced.

The target thicknesses expressed in (nuclei per μb)$\times10^{-7}$ are summarized in Table I. The thicknesses in radiation lengths are all near $0.1X_0$ so that the photon attenuation in different targets is similar. Roughly 10% of the photons are absorbed electromagnetically in the full-target thickness so that, on the average, 95% of the photons are available to produce hadronic interactions. More explicitly, the average photon transmission prior to a a hadronic interaction is given by

$$\frac{n(T,\mu)}{n(0,\mu)}=\frac{\int_0^T e^{-\mu L}dL}{\int_0^T dL}=\frac{1-e^{-\mu T}}{\mu T}, \tag{11}$$

where μ is the photon attenuation coefficient.[14] Calculated values of the average photon transmission for this experiment are also given in Table I.

G. Electronic Logic and Data Storage

The electronic logic has been described in detail elsewhere.[11] The logic was arranged so that a tagged photon $T\bar{A}$ was specified by one and only one twofold coincidence in the four tagging channels during the accelerator gate and with no simultaneous signal from any of the anticounters $A0$ through $A4$. An event required (1) $T\bar{A}$, a tagged photon, (2) $\bar{S}1$, the absence of a large pulse in the forward electromagnetic counter, and (3) evidence for the production of at least one hadron, i.e., $S2$. The $S2$ signal was an inclusive *OR* of the fourfold coincidences of the four planes of $S2a$ or $S2b$, or the summed pulse height $\Sigma S2$ of the eight planes. The threshold on the $\Sigma S2$ signal was typically 1 GeV of shower energy or the equivalent of one minimum-ionizing particle through 12 planes. The on-line event signal was then $T\bar{A}S\bar{1}S2$, but event candidates were recorded if they satisfied the far less restrictive criteria $T\bar{A}S\bar{1}$ or $T\bar{A}S2$ corresponding to a tagged photon plus *either* (2) or (3) above.

Each candidate that was recorded included the following information: The pulse heights of the eight $S2$ scintillator planes and $S1$, gated latch information on the tagging channel and the fast coincidences, and the relative timing of the $T\bar{A}S\bar{1}$ and $S2$ signals as measured by a time-to-digital converter. With this information, the experiment could be replayed with the computer with different discriminator thresholds, different $S2$ coincidence criteria, etc.

The most important accidental occurred between false tags, a major portion of the $T\bar{A}S\bar{1}$ signal, and $S2$. To monitor this accidental rate, two circuits having resolving times of 10 and 15 nsec registered coincidences between these two signals. In addition, the coincidence rate with the $S2$ signals delayed by 64 nsec was also monitored. The rate of accidental vetoing of good events by $S1$ was monitored by the circuit

$$T\bar{A}(S1)_{33}(\bar{A})_{33}(\bar{T})_{33}\equiv S1\,V,$$

TABLE I. Parameters for the various targets used (e.g., Pb and PbE are targets employed in different lead data runs).

	Target thickness [(nuclei/μb)$\times10^{-7}$]	Average photon transmission
H[a]	42.94± 0.08	0.9576± 0.0006
D[a]	50.04± 0.08	0.9504± 0.0006[b]
C I	21.66± 0.06	0.9625± 0.0006
C II	21.93± 0.06	0.9623± 0.0006
C I + C II	43.59± 0.09	0.9259± 0.0008
Cu I	0.8639± 0.0004	0.9735± 0.0003
Cu II	0.8711± 0.0004	0.9733± 0.0003
Cu I + Cu II	1.7350± 0.0006	0.9474± 0.0004
Pb	0.2905± 0.0001	0.9419± 0.0004
PbE	0.4061± 0.0004	0.9280± 0.0006

[a] Hydrogen and deuterium values are only present as examples since the density is temperature dependent. Values shown are for a hydrogen density of 0.0708 g/cm^3 and a deuterium density of 0.165 g/cm^3.

[b] Only the charged portion of the deuteron contributes to the photon attenuation.

where the three signals $S1$, $\bar{A}$, and $\bar{T}$ were delayed by 33 nsec so as to measure the accidental vetoes of incident photons by $S1$. This rate was actually quite low, ~1%, due to the presence of the veto counters $A3$ and $A4$.

Readout time in the electronics was accounted for by the data gate which vetoed the $T\bar{A}$ signal starting 10 nsec after the arrival of the trigger signals $T\bar{A}S\bar{1}$ or $T\bar{A}S2$. The veto lasted until the ADC's and gated latches were reset after the data had been strobed into the 120-bit buffer which was used to transmit the data to the magnetic tape. Also, the electronics was made "deadtimeless" so that as the beam rate increased, the logic responded by shutting off, rather than by becoming inefficient in the veto channels.

III. DATA, CORRECTIONS, AND UNCERTAINTIES

The raw total cross section for photon absorption on a nucleus A is calculated from

$$\sigma_R^A = \frac{1}{N}\frac{E}{M} \tag{12a}$$

$$\approx \frac{1}{N}\frac{T\bar{A}S\bar{1}S2}{T\bar{A}}, \tag{12b}$$

where N is the number of target nuclei per unit area as given in Table II, M [or "monitor" ($\approx T\bar{A}$)] is the number of incident photons, and E [or "events" ($\approx T\bar{A}S\bar{1}S2$)] is the number of photons interacting hadronically. Corrections were applied to M to account for beam attenuation in the target and also for the false tags included in the signal $T\bar{A}$. Corrections to the numerator included (1) accidentals, (2) empty-target background, (3) pair contamination, (4) geometric losses, and (5) $S2$ detection inefficiency.

The true number of incident photons, M, was found as follows: In place of $T\bar{A}$ the combination $(T\bar{A}S1 + T\bar{A}S\bar{1}S2 - 0.6S1\,V)$ was used, since it was free of false tags. In this expression, the first term is the number of incident photons passing through the target or producing pairs, the second term is the number interacting hadronically, and the third term takes into account accidental $S1$ coincidences with $T\bar{A}$ (the 0.6 factor arising from coincidence-width considerations). This three-term expression was then multiplied by the correction shown in Table I to account for the attenuation in the target of the incident photon beam.

Accidental coincidences (a_0) in the event signal $T\bar{A}S\bar{1}S2$ resulted from false tags (given approximately by $T\bar{A}S\bar{1}$) which occurred during spurious hadron signals, $S2$. The corrected hadron event rate was then

$$E = T\bar{A}S\bar{1}S2 - a_0. \tag{13}$$

Three methods were used to estimate the accidentals rate a_0: (1) linear extrapolation to zero $S2$ pulse width of data taken simultaneously with 10-nsec and 15-nsec $S2$ pulse widths, (2) scaling coincidences between $T\bar{A}S\bar{1}$ signals and the 10-nsec and 15-nsec $S2$ signals delayed by 64 nsec, and (3) examination of the relative timing between $T\bar{A}S\bar{1}$ and $S2$ for each event recorded on magnetic tape. The three methods were consistent within ±20%, and a systematic error of ±20% of a_0 was therefore assigned. Estimates of the average accidentals in $T\bar{A}S\bar{1}S2$ for each target are given in Fig. 9(a) as a function of central photon energy. The accidental correction is seen to be relatively large on nuclei of high Z. The accidentals corrections were applied to individual tagging channels by using the fact that the accidentals were proportional to the false-tag rates.

The measured empty-target rates for the liquid-target and solid-target configurations, respectively 4.08 ± 0.43 and 2.81 ± 0.55 per 10^5 incident photons, were essentially independent of energy and of tagging channel. The corresponding uncertainties did, however, vary somewhat with channel

TABLE II. Corrected total cross sections averaged for four tagging channels for a fixed positron energy. The errors include statistical and averaged systematic contributions.

E_γ (GeV)	$\sigma_T(\gamma p)$ (μb)	$\sigma_T(\gamma d)$ (μb)	$\sigma_T(\gamma C)$ (μb)	$\sigma_T(\gamma Cu)$ (μb)	$\sigma_T(\gamma Pb)$ (μb)
4.1± 0.5	131.4± 2.7	242.4± 4.7	1305± 52	5983± 393	16 680± 1960
5.2± 0.6	128.1± 2.4	237.1± 4.2	1288± 38	5968± 351	...
6.6± 0.8	121.9± 2.2	238.5± 5.6	1278± 34	5948± 359	16 760± 1320
8.4± 1.0	120.0± 2.2	234.9± 4.8	1238± 32	5305± 314	14 930± 1330
9.8± 1.2	120.4± 2.2	231.3± 3.5	1219± 62	...	...
10.7± 1.3	123.6± 2.2	225.0± 3.5	1218± 35	...	...
12.5± 1.5	117.7± 2.2	223.6± 3.8	1161± 31	...	...
13.6± 1.6	114.6± 2.5	219.7± 3.0	1124± 38	5380± 353	12 870± 2200
16.4± 2.0	113.6± 2.6	217.2± 4.2	1171± 30	5228± 352	15 240± 1860

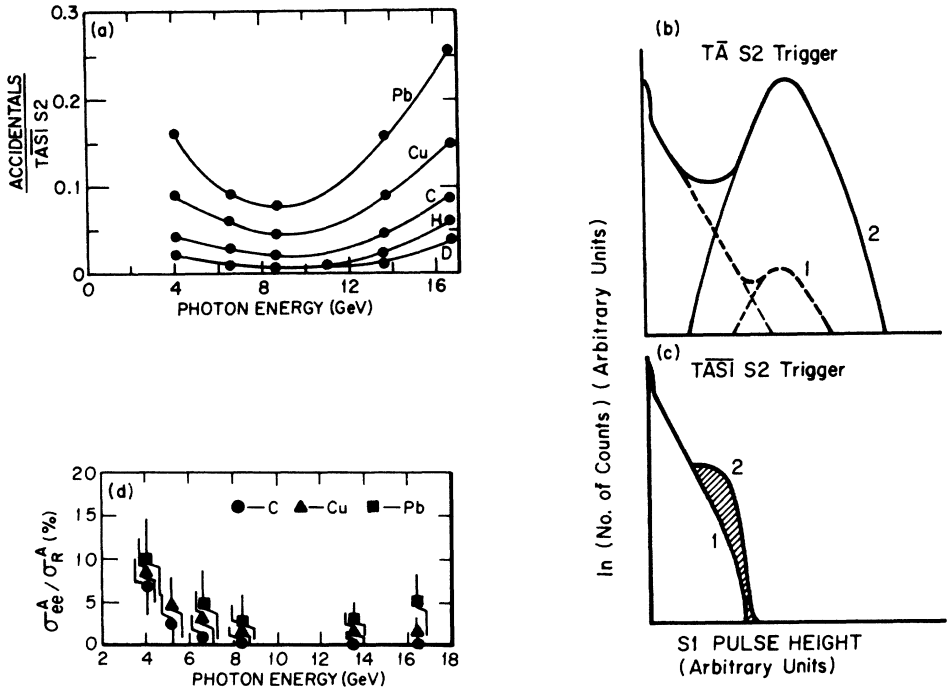

FIG. 9. (a) Average accidental rates in the $TA\bar{S}1S2$ signal for each target and energy. (b) Logarithmic $S1$ pulse-height spectra for the rudimentary hadron trigger $TAS2$. Normal hadronic events yielded low pulse heights in $S1$, while the pair background events appeared as a peak centered just below the incident energy. The background peak was much larger relative to the hadron signal for high-Z targets (curve 2) than for low-Z targets (curve 1). (c) Same as (b) except that the $S1$ spectrum was cut off by requiring $\bar{S}1$ in the trigger. (d) Corrections for positron-electron pairs. This correction was negligible for hydrogen and deuterium in the normal geometry.

number as a result of differences in accidentals rates. The errors given above are for the worst cases. The empty-target corrections were made by subtracting the appropriate empty-target rate from the full-target rate $TA\bar{S}1S2/TA$ corrected for accidentals, photon attenuation, etc.

Events faked by pairs occurred almost entirely when the wider-angle member was detected in $S2$ while the more forward member failed to trigger the $S1$ discriminator. The *logarithm* of the number of counts versus the $S1$ pulse height is shown in Fig. 9(b) for the rudimentary hadron trigger $TAS2$. Normal hadronic events yielded low pulse heights in $S1$, while the pair background events appear in this figure as a peak centered just below the incident photon energy. The background peak was much larger relative to the hadron signal for the high-Z targets, since pair production varies as Z^2 while the hadronic photon absorption varies only as $A^{0.9}$. The effect of the $S1$ discriminator was to cut off the $S1$ pulse-height spectrum as shown in Fig. 9(c). This eliminated most of the pair background while preserving nearly all of the hadron signal. The magnitude of the background remaining in $TA\bar{S}1S2$ could be estimated from the shaded region of Fig. 9(c), so that a suitable correction could be made. This correction was negligible for hydrogen and deuterium. The corrections for carbon, copper, and lead are plotted in Fig. 9(d). The validity of this method for correcting the pair background was verified by enhancing the background peak by taking data with $S2b$ downstream of its standard position, so that particles close to the beam line were intercepted.

Geometric losses occurred, because the $S2$ solid angle was less than 4π. The losses were negligible for complex nuclei and for multi-particle events in all cases. For the extended hydrogen and deuterium targets, the losses were also negligible except for single-particle production in the lowest tagging channel and at the lowest photon energies. Monte Carlo calculations, based on the measured t distributions for various single-particle production processes on nucleons[15] and nuclei,[16] yielded net corrections of 2.7 ± 1.0 μb $\lesssim 2\%$ in the worst case. These corrections were consistent with geometrical tests described in Sec. II E.

Because the $S2$ counters were not 100% efficient for hadrons below about 2 GeV (recall Fig. 6), corrections had to be made for cases in which the summed pulse height $\Sigma S2$ was less than the required 1 GeV (12 tracks) and in which no particle

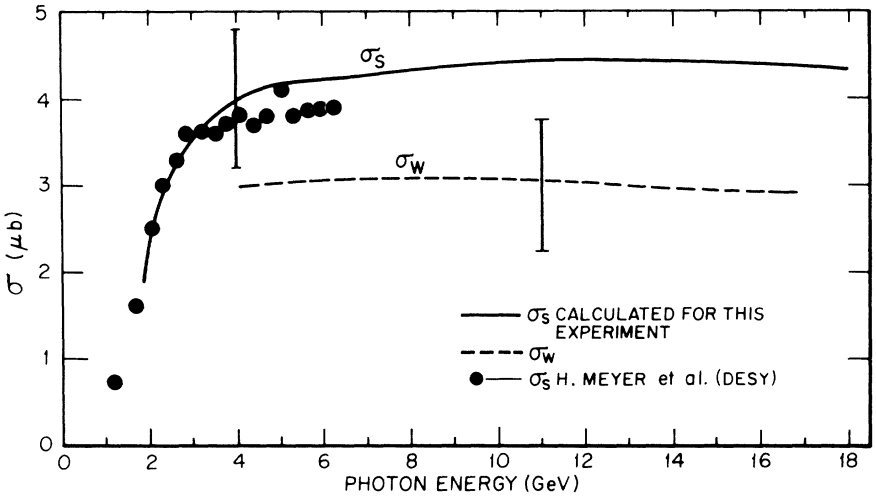

FIG. 10. Glauber correction calculated for this experiment compared with the correction used in Ref. 19 and with the additional West correction.

was sufficiently penetrating to make a fourfold coincidence in either $S2a$ or $S2b$. This could occur, for example, when a photon having only a few GeV divided its energy more or less uniformly among a number of final-state hadrons. In such a case, of the hadrons intercepting the $S2$ counter, none might penetrate all four layers of lead, and the total pulse height might be insufficient to trigger the $\Sigma S2$ discriminator. An estimate of this loss was made from test data taken with a lead target and with the first lead plate of $S2a$ removed. The tape record for the $T\overline{A}S\overline{1}$ trigger then permitted a computer scan for events with a pulse height in the first, unshielded $S2a$ plane equivalent to five or more particles and with little or no pulse height in the shielded planes. This topology, averaged over the four tagging channels, amounted to $(0.3 \pm 0.2)\%$ of the raw lead cross section at the lowest (worst case) positron energy. A similar scan with the normal data geometry allowed the probabilities for threefold and fourfold coincidences in $S2a$ or $S2b$ to be compared. This resulted in an estimate of the fourfold inefficiency that was independent of target material and that varied from $(1.3 \pm 0.5)\%$ to $(0.5 \pm 0.5)\%$ in going from the lowest to the highest incident positron energies.

The total cross section for a particular target nucleus and energy was calculated from

$$\sigma_T(\gamma A) = \sigma_R^A - \sigma_{ee}^A + \sigma_{\text{geom}}^A + \sigma_I^A + \sigma_{\text{res}}^A , \tag{14}$$

where σ_R^A was the raw cross section given by Eq. (12) corrected only for accidentals in $T\overline{A}S\overline{1}S2$, for false tags and photon attenuation in $T\overline{A}$, and for empty-target backgrounds, and where σ_{ee}^A was the pair background, σ_{geom}^A was the geometric loss in $S2$, σ_I^A was the $S2$ inefficiency correction, and $\sigma_{\text{res}}^A = (0.4\% \pm 0.2\%)\sigma_R^A$ resulted from the residual gas in the empty deuterium or hydrogen target. The uncertainties in the various components of σ_T were combined in quadrature to give the final error.

Neutron cross sections were found from the hydrogen and deuterium cross sections using the equation

$$\sigma_T(\gamma n) = \frac{\sigma_T(\gamma d)}{1-\beta} - \sigma_T(\gamma p) + \sigma_S , \tag{15}$$

where $\sigma_S \approx 4$ μb is the Glauber correction[17,18] for shadowing of one nucleon by the other in the deuterium nucleus, and the $(1-\beta)^{-1}$ factor accounts for Fermi motion of these nucleons. The Glauber correction calculated for this experiment[11] versus photon energy is shown in Fig. 10. Also shown is the Glauber correction obtained from the tables given by Meyer *et al.*[19] The two estimates agree well within the 20% error assumed for our calculation. It has recently been shown by West[20] that, in addition to the Glauber correction, a correction must also be made for the Fermi motion of the particles in the deuteron. This correction has been computed by Dominguez, Gunion, and Suaya,[21] using various wave functions for the deuteron. They express their results in terms of a smearing correction β which has a value of typically $(1.3 \pm 0.3) \times 10^{-2}$ and is nearly energy-independent above 4 GeV and rather insensitive to the particular wave-function chosen. With the West correction defined as

$$\sigma_W \equiv \frac{\sigma_T(\gamma d)}{1-\beta} - \sigma_T(\gamma d) \approx \beta\, \sigma_T(\gamma d) , \tag{16}$$

the neutron cross section is given by

$$\sigma_T(\gamma n) = \sigma_T(\gamma d) - \sigma_T(\gamma p) + \sigma_S + \sigma_W . \tag{17}$$

The values which we have used for the West cor-

TABLE III. Proton and deuteron cross sections and cross sections obtained from them. The neutron cross section has been obtained using both Glauber and West corrections ($\sigma_S+\sigma_W$ shown). The sum and difference of the proton and neutron cross sections are derived from $\sigma_T(\gamma p)$ and $\sigma_T(\gamma d)$ so as to reduce systematic errors. E_0 is the energy of the incident positron producing the bremsstrahlung photons of energy E_γ ($\pm 0.025\, E_0$). Every fifth row is the average over the previous four tagging energies.

E_0 (GeV)	E_γ (GeV)	$\sigma_T(\gamma p)$ (μb)	$\sigma_T(\gamma d)$ (μb)	$\sigma_S+\sigma_W$ (μb)	$\sigma_T(\gamma n)$ (μb)	σ_{p+n} (μb)	σ_{p-n} (μb)
4.84	3.70	128.4± 4.6	235.8± 8.1	6.9± 1.1	114.3± 9.1	242.7± 8.2	14.2± 11.9
	3.94	136.1± 4.9	251.1± 8.6	7.0± 1.1	121.9± 9.7	258.1± 8.7	14.2± 12.6
	4.19	132.9± 5.0	240.2± 9.0	7.0± 1.1	114.3± 10.1	247.2± 9.0	18.5± 13.2
	4.43	128.3± 5.7	244.2± 10.6	7.1± 1.1	123.0± 11.8	251.2± 10.6	5.3± 15.2
	4.07	131.4± 2.7	242.4± 4.7	7.0± 1.1	117.9± 5.2	249.4± 4.9	13.5± 6.7
6.15	4.70	126.9± 4.2	242.8± 7.4	7.1± 1.1	123.0± 8.4	249.9± 7.5	3.8± 10.9
	5.01	134.4± 4.4	229.2± 7.5	7.2± 1.1	101.0± 8.5	236.3± 7.5	32.4± 11.3
	5.32	121.7± 4.4	238.4± 8.0	7.2± 1.1	123.9± 9.0	245.6± 8.1	−2.2± 11.6
	5.63	130.1± 5.2	238.7± 9.3	7.3± 1.1	115.9± 10.5	246.0± 9.4	14.2± 13.7
	5.17	128.1± 2.4	237.1± 4.1	7.2± 1.1	116.2± 4.7	244.3± 4.9	11.9± 6.1
7.82	5.98	120.7± 4.0	250.2± 10.7	7.4± 1.2	136.8± 11.3	257.6± 7.5	−16.1± 13.1
	6.37	128.6± 4.2	233.9± 10.6	7.4± 1.2	112.7± 11.3	241.3± 7.5	15.8± 13.3
	6.76	120.1± 4.2	238.2± 10.9	7.4± 1.2	125.5± 11.3	245.6± 8.1	−5.3± 13.6
	7.16	118.0± 4.5	230.5± 11.6	7.4± 1.2	119.9± 12.3	237.9± 9.4	−1.8± 14.4
	6.57	121.9± 2.2	238.5± 5.6	7.4± 1.2	123.9± 6.0	245.9± 4.4	−2.0± 6.9
10.04	7.68	123.9± 4.0	216.5± 8.7	7.5± 1.2	100.0± 9.5	223.9± 8.7	23.9± 11.6
	8.18	121.6± 4.1	238.6± 9.3	7.5± 1.2	124.5± 10.0	246.1± 9.3	−2.9± 12.2
	8.68	119.2± 4.2	243.8± 9.4	7.5± 1.2	132.1± 10.3	251.4± 9.5	−12.9± 12.4
	9.19	114.9± 4.4	245.7± 10.1	7.5± 1.2	138.2± 10.9	253.2± 10.1	−23.3± 13.2
	8.43	120.0± 2.2	234.9± 4.8	7.5± 1.2	122.4± 5.2	242.4± 5.0	−2.5± 6.3
11.71	8.95	122.5± 4.1	242.3± 6.6	7.5± 1.2	127.3± 7.7	249.8± 6.7	−4.8± 10.3
	9.54	123.5± 4.2	218.2± 6.5	7.5± 1.2	102.2± 7.6	225.7± 6.5	21.2± 10.3
	10.12	122.2± 4.2	226.2± 6.6	7.5± 1.2	111.6± 7.8	233.8± 6.7	10.7± 10.5
	10.71	112.1± 4.6	220.5± 7.0	7.4± 1.2	115.8± 8.2	227.9± 7.1	−3.7± 11.3
	9.83	120.4± 2.2	231.3± 3.5	7.5± 1.2	118.4± 4.1	238.8± 3.7	2.1± 5.5
12.75	9.75	117.1± 4.0	223.0± 6.2	7.5± 1.2	113.4± 7.3	230.5± 6.3	3.7± 9.9
	10.39	128.1± 4.3	236.0± 6.6	7.4± 1.2	115.3± 7.7	243.4± 6.6	12.8± 10.5
	11.03	127.9± 4.4	231.3± 6.6	7.4± 1.2	110.8± 7.8	238.7± 6.6	17.2± 10.8
	11.67	122.2± 4.6	208.4± 6.9	7.4± 1.2	93.6± 8.1	215.8± 6.9	28.5± 11.2
	10.71	123.6± 2.2	225.0± 3.5	7.4± 1.2	108.8± 4.1	232.4± 3.7	14.7± 5.5
14.87	11.38	121.4± 4.0	223.0± 7.1	7.4± 1.2	109.1± 8.1	230.5± 7.2	12.2± 10.6
	12.12	115.3± 4.0	222.9± 7.3	7.4± 1.2	115.0± 8.2	230.3± 7.3	0.3± 10.7
	12.86	116.2± 4.1	228.0± 7.4	7.4± 1.2	119.3± 8.3	235.4± 7.4	−3.1± 10.9
	13.61	117.7± 4.8	220.1± 7.8	7.4± 1.2	109.8± 9.0	227.5± 7.8	7.9± 12.0
	12.49	117.7± 2.2	223.6± 3.8	7.4± 1.2	113.4± 4.4	231.0± 4.1	4.3± 5.7
16.20	12.39	115.0± 4.5	220.9± 5.0	7.4± 1.2	113.4± 6.4	227.4± 5.1	1.6± 9.9
	13.20	111.1± 4.5	228.4± 5.1	7.4± 1.2	124.7± 6.6	235.8± 5.3	−13.6± 10.1
	14.01	119.3± 4.9	207.9± 5.1	7.3± 1.2	95.9± 6.9	215.2± 5.3	23.4± 10.7
	14.82	113.3± 5.8	222.4± 6.2	7.3± 1.2	116.4± 8.2	229.7± 6.2	−3.2± 12.8
	13.61	114.6± 2.5	219.7± 3.0	7.3± 1.2	112.4± 3.7	227.0± 3.2	2.2± 5.5
19.50	14.92	112.7± 4.2	223.1± 7.2	7.3± 1.2	117.7± 8.2	230.4± 7.3	−5.0± 10.9
	15.89	114.9± 4.5	211.1± 7.5	7.3± 1.2	103.5± 8.6	218.4± 7.5	11.5± 11.5
	16.87	112.5± 5.9	221.4± 8.6	7.3± 1.2	116.0± 10.3	228.5± 8.6	−3.5± 14.4
	17.84	115.2± 8.1	210.8± 10.3	7.3± 1.2	102.8± 13.0	218.0± 10.3	12.4± 19.0
	16.38	113.6± 2.6	217.2± 4.2	7.3± 1.2	110.8± 5.0	224.4± 4.4	2.8± 6.6

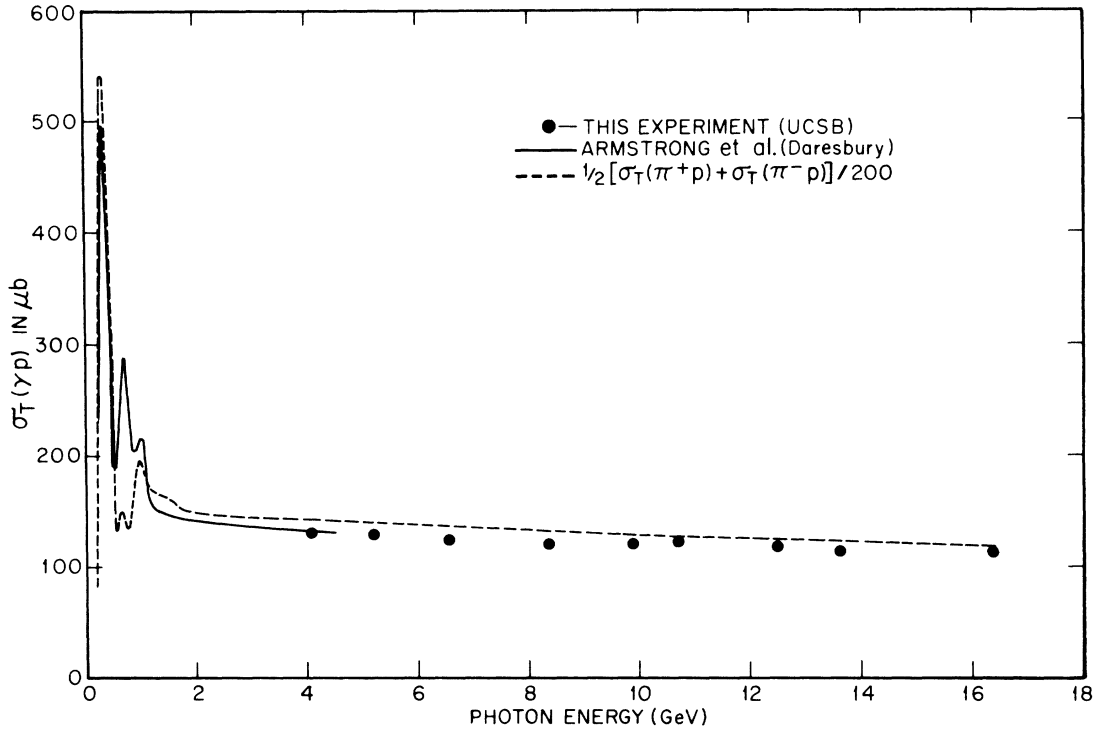

FIG. 11. Comparison of the energy dependence for total absorption of real photons and ρ mesons {given in the quark model by $\frac{1}{2}[\sigma_T(\pi^+ p) + \sigma_T(\pi^- p)]$}.

rection are also shown in Fig. 10.

Because several of the systematic errors in $\sigma_T(\gamma p)$ and $\sigma_T(\gamma d)$ cancel in computing $\sigma_T(\gamma n)$, the uncertainty in $\sigma_T(\gamma n)$ was obtained from an expansion of Eq. (17) in terms of the various constituents. The errors calculated in this way were typically 25% smaller than the errors obtained by using Eq. (17) directly.

The corrected cross sections and errors averaged over the four tagging channels are presented in Table II for hydrogen, deuterium, carbon, copper, and lead. The values and errors for $\sigma_T(\gamma p)$, $\sigma_T(\gamma n)$, $\sigma_S + \sigma_W$, σ_{p+n}, and σ_{p-n} are given for each channel in Table III. While most of these data have been reported earlier,[1,2] the results for carbon, copper, and lead in the range 3.7 to 7.4 GeV are new. There are two changes from the previously published values: The four proton data points for photons produced by 4.84-GeV positrons were in error by about 4 μb because data from a nonstandard geometry were mistakenly used, and the "West correction" has been applied to the deuteron data presented here in obtaining $\sigma_T(\gamma n)$ and the quantities

$$\sigma_{p+n} = \sigma_T(\gamma p) + \sigma_T(\gamma n) = \sigma_T(\gamma d) + \sigma_S + \sigma_W \quad (18)$$

and

$$\sigma_{p-n} = \sigma_T(\gamma p) - \sigma_T(\gamma n) = 2\sigma_T(\gamma p) - \sigma_T(\gamma d) - \sigma_S - \sigma_W . \quad (19)$$

Note again that errors for σ_{p+n} and σ_{p-n}, as with $\sigma_T(\gamma n)$, may not be found from the errors in $\sigma_T(\gamma p)$ and $\sigma_T(\gamma d)$. The experimental results are displayed graphically and compared with theoretical models in the next section.

IV. COMPARISON OF EXPERIMENT AND THEORY

A. Nucleon Data

The measured total cross sections on protons averaged over the four tagging channels are plotted versus photon energy in Fig. 11. Also shown are eyeball fits to the recent high-resolution tagged-photon data of Armstrong *et al.*[22] at Daresbury, and the mean of $\pi^+ p$ and $\pi^- p$ total cross sections divided by 200. The two tagged-photon experiments agree extremely well in the region around 4 GeV where they overlap, and they are, in fact, consistent within their quoted errors. The mean of the $\pi^+ p$ and $\pi^- p$ total cross sections divided by 200 also agrees within about ±10% over the full energy range except in the region of some of the resonances between 0.5 to 1.2 GeV. The total cross section has also been measured, using virtual pho-

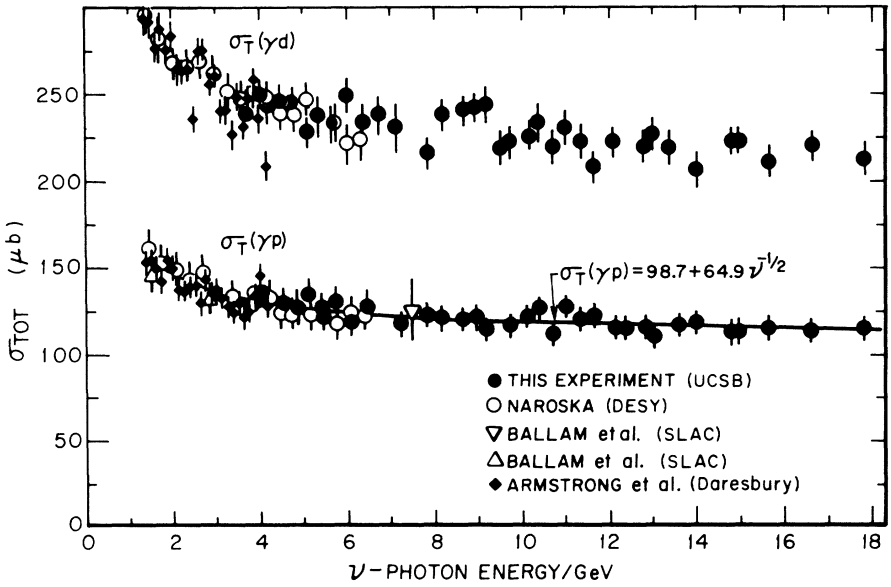

FIG. 12. The total hadronic photoabsorption cross sections measured on hydrogen and deuterium. The energy-dependent fit for $\sigma_T(\gamma p)$ is for the data of this experiment only; the fit is extrapolated to lower energy (thin line) for comparison with other data.

tons from inelastic electron scattering extrapolated to the limit $q^2 = 0$, by Bloom *et al.*[23] Within the ±10% errors of their measurements the real photon and virtual photon experiments give consistent results over the full range of data overlap, 0.265 GeV $< E_\gamma <$ 15 GeV. *In general, one may conclude that the absorptions of virtual photons and real photons are the same, and photon absorption is similar to hadron absorption reduced by a factor of 200, above the resonance region.*

The similarity in the shapes of the photoabsorption cross sections and the hadron-hadron total cross sections suggests a parametrization of the photon data as a sum of Regge-pole exchanges, which in the high-energy limit leads to

$$\sigma_T(s) = \sum_i c_i s^{\alpha_i(0)-1}, \tag{20}$$

where

$$s = M_N(M_N + 2E_\gamma)/1\ \text{GeV}^2$$

is the square of the total energy in the center-of-mass system per GeV^2, c_i is a constant, and $\alpha_i(0)$ is the $t = 0$ intercept of the angular momentum of the ith contributing trajectory. In the limit of high-energy photons, $2E_\gamma \gg M_N$, so that $s \approx 2E_\gamma/1$ GeV $= 2\nu$, where ν is the incident photon energy per GeV. By renormalizing the constants, we can thus write

$$\sigma_T(\nu) = \sum_i c_i \nu^{\alpha_i(0)-1}. \tag{21}$$

The leading trajectories with charge conjugation +1 and with isospin 0 or 1 are the P [with $\alpha_P(0) = 1$] and the P' and A_2, both of which are observed to have $\alpha(0) \approx 0.5$ in fits[24] to hadron-hadron cross sections at high energies. The total cross sections may then be expanded as

$$\sigma_T(\gamma p) = c_P + (c_{P'} + c_{A_2})\nu^{-1/2}, \tag{22}$$

$$\sigma_T(\gamma n) = c_P + (c_{P'} - c_{A_2})\nu^{-1/2}, \tag{23}$$

so that

$$\tfrac{1}{2}[\sigma_T(\gamma p) + \sigma_T(\gamma n)] = c_P + c_{P'}\nu^{-1/2}, \tag{24}$$

$$\tfrac{1}{2}[\sigma_T(\gamma p) - \sigma_T(\gamma n)] = c_{A_2}\nu^{-1/2}. \tag{25}$$

The separate contributions of the Pomeranchukon P, the P', and the A_2 can thus be determined from fits to the data in the form σ_{p+n} and σ_{p-n}. The proton and neutron cross sections can also be conveniently parametrized as

$$\sigma_T(\gamma p) = a^p + b^p\nu^{-1/2}, \tag{26}$$

$$\sigma_T(\gamma n) = a^n + b^n\nu^{-1/2}. \tag{27}$$

The measured proton and deuteron total cross sections for each tagging channel are compared in Fig. 12 with data from two bubble-chamber experiments,[25] the Daresbury experiment,[22,26] and a third tagged-photon counter experiment performed at DESY.[19] The data are in excellent agreement. The energy-dependent fit of Eq. (26) to the data of this experiment extrapolates nicely through the lower-energy data.

In Fig. 13 the neutron total cross sections and the differences σ_{p-n} of the proton and neutron cross

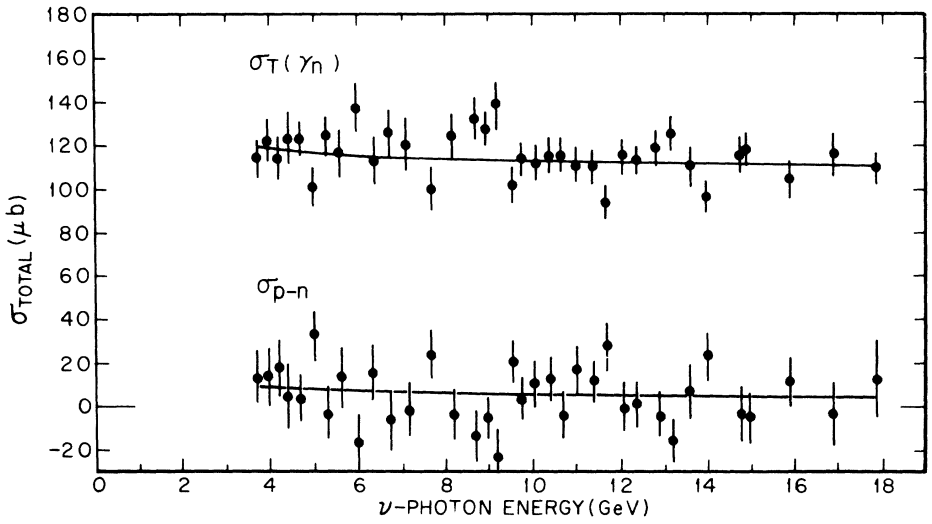

FIG. 13. Neutron total cross sections and proton-neutron total-cross-section differences derived from the measured rates on hydrogen and deuterium with calculated Glauber and West corrections. The energy-dependent fits discussed in the text are also shown.

sections of this experiment, as well as the energy-dependent fits of Eqs. (25) and (27) to the data are presented. The data are internally consistent, and the χ^2's per degree of freedom for the Regge parametrizations are in the range 0.9 to 1.1. The hypothesis that $\sigma_T(\gamma p) = \sigma_T(\gamma n)$ in our energy range has a χ^2 probability of only 5%. The application of the West correction has reduced the statistical significance of the proton-neutron difference, since the χ^2 probability for the fit with $\sigma_T(\gamma p) = \sigma_T(\gamma n)$ was previously 0.3%.[2] A constant difference leads to a χ^2 probability of 18%, while the Regge parametrization of Eqs. (26) and (27) in terms of two distinct nucleons has a probability of 25%. *The Regge-pole formulation provides an acceptable parametrization of the photon absorption on protons and neutrons. The proton and neutron cross sections differ by about 6 μb in the region from 3.7 to 18.3 GeV.*

The values of the Regge-pole parameters in μb are summarized in Table IV, along with the proton and neutron total cross sections and the ratio of isovector-to-isoscalar contributions from the energy-dependent term $c_{A_2}/c_{P'}$. This ratio is calculated from the values of the σ_{p+n} and σ_{p-n} fits, rather than from the $\sigma_T(\gamma p)$ and $\sigma_T(\gamma n)$ fits, to minimize the effects of correlated errors. The present result, 0.18 ± 0.06, differs only slightly from that published earlier,[2] 0.19 ± 0.05, because of two compensating changes: (1) the four proton data points obtained with photons from 4.84-GeV positrons, as discussed at the end of Sec. III, and (2) the application of the additional West correction.

The existence of an A_2 contribution, which gives the energy dependence in σ_{p-n}, has been predicted by Harari[27] in a calculation of the proton-neutron mass difference. From group-symmetry arguments and the values of the γ_ρ and γ_ω coupling constants, Wada[28] has obtained a value of $c_{A_2}/c_{P'} = 0.30$, not quite consistent with the experimental result. Rosner[29] has pointed out that the Fox and Freedman[30] analysis of the Compton amplitude with finite-energy sum rules and the measurements of single-pion photoproduction lead to a prediction of the proton and neutron cross sections. For $\alpha_{A_2}(0) = 0.5$, the calculated result[31] is $\sigma_{p-n} = (20.5 \pm 7.2)\nu^{-1/2}$ μb, in agreement with the experimental value of $(18.3 \pm 6.1)\nu^{-1/2}$ μb.

The fits which have been presented do not include lower-energy data from other experiments. Fits including all of the data above 2 GeV have been made,[21] with results that are consistent with those of Table IV. These fits demonstrate the difficulty in determining the ratio $c_{A_2}/c_{P'}$ given by the energy dependence of the proton-neutron difference. With all of the data included the value obtained is

TABLE IV. Fits to the nucleon data in the manner of hadronic Regge fits, using the form $\sigma = a + b\nu^{-1/2}$, where ν is the photon energy per GeV. Also given are the corresponding contributions for the Pomeranchukon (c_P) and the energy-dependent isoscalar ($c_{P'}$) and isovector (c_{A_2}) contributions obtained from both the proton and neutron data.

$a^p = 98.7 \pm 3.6$ μb	$\sigma_T(\gamma p) = (98.7 + 65.0\nu^{-1/2})$ μb
$b^p = 65.0 \pm 10.1$ μb	
$a^n = 103.4 \pm 6.7$ μb	$\sigma_T(\gamma n) = (103.4 + 33.1\nu^{-1/2})$ μb
$b^n = 33.1 \pm 19.4$ μb	
$c_P = 101.9 \pm 2.9$ μb	$\sigma_T(\gamma p) - \sigma_T(\gamma n) = (18.3 \pm 6.1)\nu^{-1/2}$ μb
$c_{P'} = 50.9 \pm 8.5$ μb	
$c_{A_2} = 9.1 \pm 3.0$ μb	$c_{A_2}/c_{P'} = 0.18 \pm 0.06$

0.13.[21] As a final comment about the fits we note that the data are not sufficiently accurate to exclude expressions such as

$$\sigma_T(\gamma\rho) = a + b\nu^{-1}, \tag{28}$$

as suggested by suri and Yennie,[31] or

$$\sigma_T(\gamma p) = a + b\nu^{-1/2} + c\nu^{-3/2}, \tag{29}$$

as predicted by Shibasaki *et al.*[32]

Damashek and Gilman[33] and Dominguez *et al.*[34] have shown that in the Regge-pole model, the dispersion relations for Compton scattering seem to require an extra real constant, in addition to that which the Regge fit to $\sigma_T(\gamma p)$ predicts. This constant is consistent with the Thomson limit $-\alpha/M$ and could correspond to a fixed pole with $J=0$, as predicted by Creutz, Drell, and Paschos.[35] Dominguez, Gunion, and Suaya[21] have made a similar analysis for the neutron data and for this case find that the value for the extra constant is consistent with zero, again like the Thomson limit, but not as expected from a parton model of the neutron. The dispersion relations imply that the Compton amplitude has an appreciable real part, the ratio of real to imaginary parts, η, varying between roughly -0.33 at 4 GeV and -0.16 at 16 GeV.[33] The vector-dominance model predicts a ρ-photoproduction amplitude with the same ratio of real and imaginary parts.

The total cross section $\sigma_T(\gamma p)$ can be compared with Compton scattering measurements using Eq. (6). As mentioned,[5] this relation involves the assumption that the part of the amplitude corresponding to scattered photons with linear polarization perpendicular to that of the incident photon is negligible. The predictions for the Compton cross section, based on the measurements of σ_T, are shown in Fig. 14, and agree with Compton data.[36] The comparisons are made with and without the effect of the real part as calculated by Damashek and Gilman.[33]

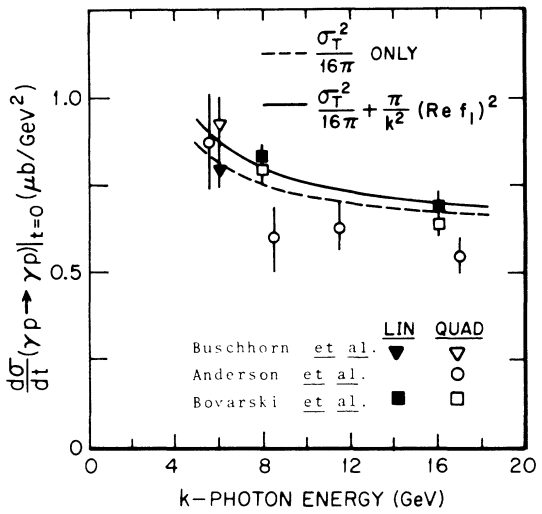

FIG. 14. Comparison between the extrapolated forward Compton-scattering differential cross sections and the predictions from the data of this experiment using the optical theorem and dispersion calculations. LIN and QUAD refer to linear-exponential and quadratic-exponential fits to the t dependence of the Compton-scattering data.

B. Comparison of the Proton Data with Vector-Meson Dominance

The vector-dominance prediction of Eq. (7) for our data on protons is plotted in Fig. 15, using an energy-dependent η_ρ, as determined from $\sigma_T(\gamma p)$ with dispersion relations by Damashek and Gilman.[33] The upper band in the figure results from assuming the ω and ϕ contributions to $\sigma_T(\gamma p)$ are (20 ± 2) μb and using $\gamma_\rho{}^2/4\pi = 0.64 \pm 0.06$, as found in a recent Orsay colliding-beam experiment,[37] while its width indicates the uncertainties in the calculation. This prediction clearly disagrees with the experimental measurements[38] of ρ photoproduction plotted. The extent of the disagreement with vector dominance can be estimated by adjusting $\gamma_\rho{}^2/4\pi$ in Eq. (7) to fit the ρ-photoproduction data. The result, indicated by the lower band in Fig. 15, is $\gamma_\rho{}^2/4\pi = 0.37 \pm 0.03$ which differs from the colliding-beam result by 4 standard deviations. As further evidence of this discrepancy, a comparison[39] of the differential cross section for ρ photoproduction on deuterium with our results on $\sigma_T(\gamma d)$ gives $\gamma_\rho{}^2/4\pi = 0.30 \pm 0.03$. *Vector dominance is not quantitatively successful in relating photon absorption data to data on the coupling constants and on vector-meson photoproduction.*

Among the possible explanations for the failure of Eq. (7) to relate the measured values of $\sigma_T(\gamma p)$, $d\sigma(\gamma p \to \rho p)/dt|_{t=0}$, and $\gamma_\rho{}^2/4\pi$ are the following:

(1) The coupling constant $\gamma_\rho{}^2/4\pi$ varies with photon mass so that the colliding-beam values on the ρ mass shell are different from the total-cross-section values on the photon mass shell.

(2) Some fraction χ of the total cross section $\sigma_T(\gamma p)$ is not mediated by the ρ, ω, and ϕ mesons.

The second possibility implies an additional interaction which may result, for instance, from the direct coupling of the bare photon[31] to nucleon constituents or from the existence of new vector mesons of higher mass m_V.[17] Adding a term $\chi\sigma(\gamma p)$ to the right-hand side of Eq. (7), the VMD prediction, produces the lower band of Fig. 15 when $\chi = 0.20 \pm 0.02$. Fortunately, the data on complex nuclei are able to distinguish between the alterna-

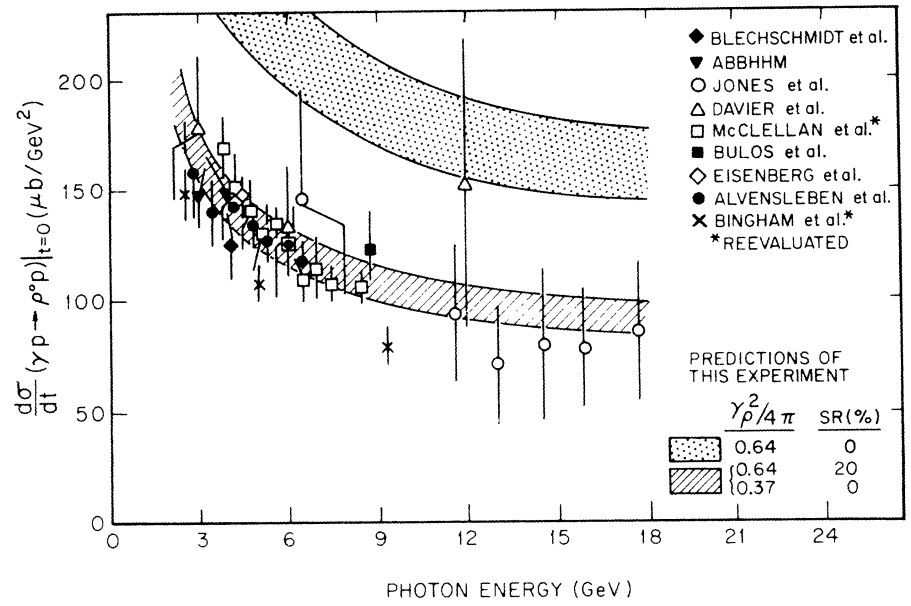

FIG. 15. Comparisons between the extrapolated forward ρ-photoproduction differential cross sections and the predictions from $\sigma_T(\gamma p)$ of this experiment using the vector-dominance model. The ω and ϕ contributions to $\sigma_T(\gamma p)$ are assumed to be 20 ± 2 μb. The dotted band is the predicted value using pure vector dominance and the colliding-beam value of 0.64 for $\gamma_\rho^2/4\pi$. Agreement between the two types of experiments is possible (shaded band) (1) if $\gamma_\rho^2/4\pi$ is assumed to be 0.37 ± 0.03 or (2) if $\gamma_\rho^2/4\pi = 0.64$ and $\sigma_T(\gamma p)$ is assumed to have a 20% contribution from short-range interactions.

tives of a coupling constant that depends on photon mass and a photoabsorption total cross section of which 20% is not associated with the ρ, ω, and ϕ.

C. Data on Complex Nuclei

The total hadronic cross sections on carbon, copper, and lead from Table II are plotted in Fig. 16. Also shown are the total cross sections on carbon and copper measured at DESY.[19] As in the case of nucleons, the data on complex nuclei from the two experiments are consistent within the assigned errors.

We noted in Sec. I that our optical-model calculations[8,11] for complex nuclei take into account the energy dependence in η_ρ (Ref. 33) and in

$$\sigma_T(\rho p) = \tfrac{1}{2}[\sigma_T(\pi^+ p) + \sigma_T(\pi^- p)] .$$

As in the deuteron, the Fermi motion of the nucleons requires that a *nuclear* West correction be applied in comparisons with optical-model calculations for complex nuclei. Lacking a proper calculation of the nuclear West effect, we have applied the *deuteron* correction factor $1/(1-\beta)$, with $\beta = 0.013$, to the *nuclear* cross sections before computing A_{eff} [as defined by Eqs. (9) and (10)], and estimated the error as equal to the whole correction, $\pm 1.3\%$. We note that the West correction has been applied in obtaining the neutron cross sec-

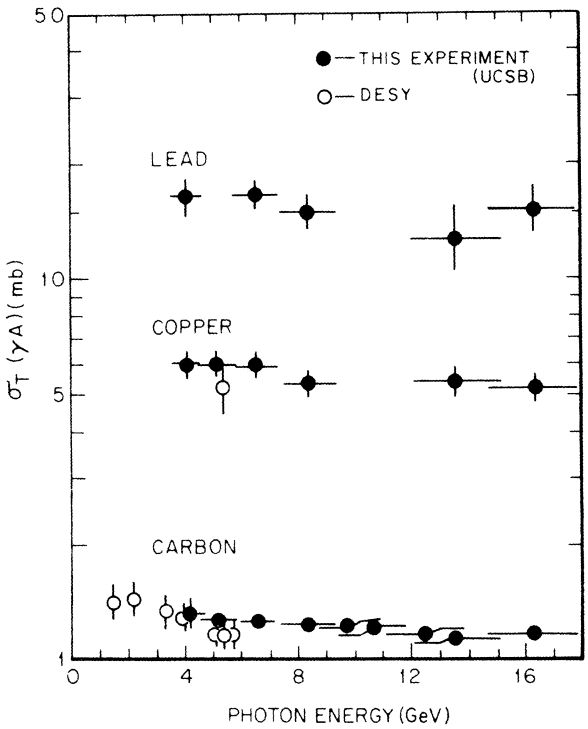

FIG. 16. The carbon, copper, and lead total cross sections of this experiment compared with data on carbon and copper from DESY.

TABLE V. Energy dependence of the effective nucleon number, A_{eff}, and the effective attenuation, A_{eff}/A (in %), for each of the targets with atomic number $Z > 1$ measured in this experiment. The average nucleon cross section used is defined as $\sigma_T(\gamma N) = (2Z/A - 1)\,\sigma_T(\gamma p) + (1 - Z/A)\,\sigma_{p+n}$ (see text for details).

E_γ (GeV)	$A_{\text{eff}} = \sigma_T(\gamma A)/\sigma_T(\gamma N)$ Carbon	Copper	Lead	A_{eff}/A (%) Carbon	Copper	Lead
4.1± 0.5	10.5± 0.4	48.4± 3.3	136.9± 16.1	87.6± 3.7	76.4± 5.1	65.3± 7.7
5.2± 0.6	10.6± 0.3	49.4± 3.0	•••	88.5± 2.9	77.9± 4.7	•••
6.6± 0.8	10.8± 0.3	50.3± 2.6	142.4± 11.3	89.7± 2.7	79.3± 4.1	68.5± 5.4
8.4± 1.0	10.6± 0.3	45.7± 2.7	129.2± 11.6	88.6± 2.5	72.1± 4.3	62.2± 5.6
9.8± 1.2	10.6± 0.5	•••	•••	88.2± 4.5	•••	•••
10.7± 1.3	10.6± 0.3	•••	•••	88.7± 2.8	•••	•••
12.5± 1.5	10.3± 0.3	•••	•••	85.4± 2.5	•••	•••
13.6± 1.6	10.0± 0.3	47.9± 3.2	115.0± 19.7	83.1± 3.1	75.5± 5.0	55.3± 9.5
16.4± 2.0	10.5± 0.3	47.0± 3.2	137.5± 16.9	87.5± 2.6	74.1± 5.0	66.1± 8.1

tions which are part of the denominator of $A_{\text{eff}} = \sigma(\gamma A)/\sigma(\gamma N)$. Values of A_{eff} and A_{eff}/A are given in Table V. Figure 17, in which A_{eff}/A is plotted versus photon energy for carbon, copper, and lead illustrates how the energy dependence of $\sigma(\rho N)$ and η_ρ serves to decrease the energy dependence of A_{eff}. Thus in our energy range we do not expect to see the diminution of shadowing which would occur when $2E_\gamma/m_\rho{}^2$ becomes shorter than the mean-free-path for ρ-nucleon interactions, λ_ρ, and indeed our data show no energy dependence in A_{eff}.

Another feature of Fig. 17 is that our data show less shadowing than is predicted by the vector-dominance calculations (solid lines). This is also apparent in Fig. 18 where the combined values of A_{eff} at different energies are plotted versus $\ln(A)$ for carbon, copper, and lead. Figure 18 also shows the predictions for no shadowing (A^1), for strong shadowing ($A^{2/3}$), and for the shadowing expected from vector meson dominance. The data fall between the no-shadowing and VMD predictions and are consistent with neither. *Photon absorption does vary more slowly with A than A^1, and therefore the photon behaves hadronically and exhibits shadowing. The shadowing is constant in the energy range 3.7 to 18.3 GeV, as expected, but is less than with vector-dominance predictions.*

The discrepancy between the vector-dominance predictions and the data cannot be explained in the case of complex nuclei by just assuming a coupling constant $\gamma_\rho{}^2/4\pi$ dependent on photon mass, since A_{eff} is nearly independent of this quantity. A fit could, however, be obtained by adjusting $\sigma_T(\rho N)$. In the region $E_\gamma > 8$ GeV, where $\sigma_T(\rho N)$ and η_ρ do

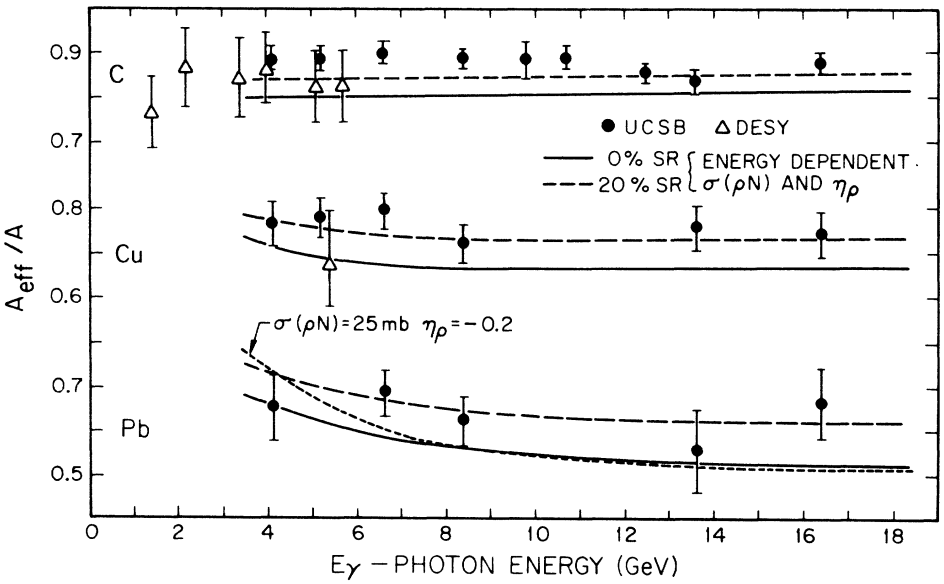

FIG. 17. The energy dependence of photon attenuation (A_{eff}/A) in carbon, copper, and lead compared with optical-model calculations using vector dominance. The solid lines are for energy-dependent $\sigma_T(\rho N)$ and η_ρ, and the dotted line is for fixed $\sigma_T(\rho N)$ and η_ρ, and the dashed lines are for vector dominance with an additional 20% short-range (SR) interaction.

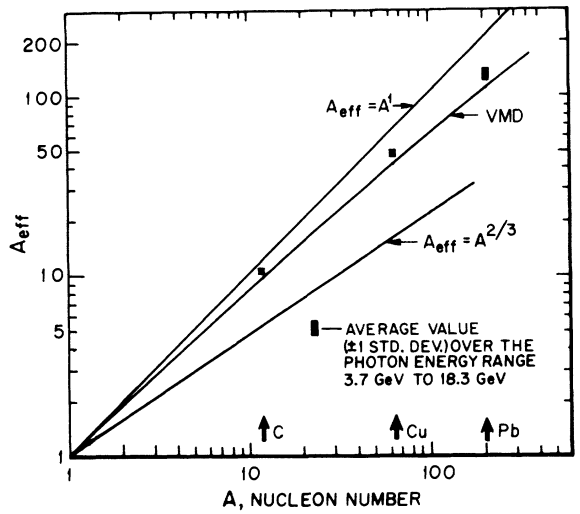

FIG. 18. Comparison of A_{eff} for carbon, copper, and lead with the limiting cases of negligible shadowing, $A_{\text{eff}} = A^1$, and strong shadowing, $A_{\text{eff}} = A^{2/3}$, as well as with the vector-meson-dominance prediction.

not vary appreciably, we would find $\sigma_T(\rho N) = (15.5 \pm 2)$ mb for $\eta_\rho = -0.2$. This is 5 standard deviations below the quark-model value, which is in agreement with other experiments.[40] Furthermore, if this value of $\sigma_T(\rho p)$ is compared with our results for $\sigma_T(\gamma p)$ through the VMD relation $\sigma_T(\gamma p) = (\alpha/4)(4\pi/\gamma_\rho{}^2)\sigma_T(\rho p)$, then $\gamma_\rho{}^2/4\pi = 0.29 \pm 0.04$, assuming a (20 ± 2) μb contribution for the ω and ϕ. Thus this resolution of the discrepancy would require *both* $\gamma_\rho{}^2/4\pi$ and $\sigma_T(\rho N)$ to be much too small, which is obviously ridiculous.

The source of the apparent disagreement between this experiment and those measuring ρ photoproduction is made even clearer if we note that $\gamma_\rho{}^2/4\pi$ as found in the latter experiments agrees remarkably well with the colliding-beam value,[37] showing *no photon-mass dependence in* $\gamma_\rho{}^2/4\pi$. Since the ρ-photoproduction experiments utilize coherence over the entire nucleus, they necessarily involve only long-range interactions, and in this case there is no disagreement with vector dominance.

The inconsistency between the $\gamma A \to \rho A$ and $\sigma_T(\gamma A)$ measurements thus requires an additional, non-vector-dominance contribution to $\sigma_T(\gamma A)$. *The additional interaction must have a range short compared to its interaction mean free path,* since it does not contribute to shadowing. Recall that to explain the relation of $\sigma_T(\gamma p)$ to ρ photoproduction we added an extra term to the VMD nucleon amplitude of magnitude $\chi\sigma_T(\gamma p)$. This same added term in the nuclear case would provide the required nonshadowing behavior, since it contributes a constant amount for each nucleon. If in the VMD optical-model calculation of $\sigma_T(\gamma A)$ this term is included with $\chi = 0.20$, which is the value used above to fix up the proton total cross section, we obtain the dashed curves in Fig. 17, in much better agreement with the data. In particular, for copper and lead the χ^2 per degree of freedom improves from 2.8 (confidence level about 10^{-3}) to 0.4 (confidence level greater than 90%), if this volume term is added. The agreement with the carbon data is also dramatically improved, but the results still are not satisfactory. However, the correlation length (l_c) used for C is the same as for Cu and Pb and really applies to nuclear matter, whereas C is nearly all surface, for which a larger[41] value of l_c would be appropriate. While a multiple scattering instead of an optical-limit calculation is necessary, we note that approximately doubling l_c gives good agreement with the C data.

Several types of interactions could account for our hydrogen results and provide the short-range behavior needed to explain the diminished shadowing on complex nuclei. One possibility[17] (which has long been recognized) is that there may be a vector meson of mass, M, sufficiently large that the distance associated with the photon's being in that virtual state $(2E_\gamma/M^2)$ is less than the mean free path, λ, of that state in nuclear matter, even at our highest energy. If such a meson should have λ comparable to that of the ρ, ω, or π, its existence would not have been manifested in our data as an increase in shadowing with energy, provided $M \gtrsim 3m_\rho$. Because its contribution to the total cross section would be about 20%, such a vector meson with $\lambda \approx \lambda_\rho$ would have to have a coupling constant $\gamma^2/4\pi \approx 6\gamma_\rho{}^2/4\pi$.

Several recent experiments have obtained data that can be interpreted as evidence for a new vector meson of mass near the upper limit that could be detected in this experiment. For example, Davier *et al.*[42] have observed a broad enhancement near 1600 MeV in the four-pion mass plot for the reaction $\gamma p \to \pi^+\pi^-\pi^+\pi^- p$, which they interpret as the dissociation of the photon into four pions. More complete observations of this four-pion bump have recently been made in a bubble chamber.[43] An enhancement in four-pion production has also been observed at a similar energy in electron-positron colliding-beam experiments at Frascati.[44] A somewhat higher-mass candidate for a vector meson has been reported[45] from antiproton annihilation. Another possibility is that there may be several higher-mass vector mesons, each making smaller contributions to the shadowing. In the spirit of the Veneziano model,[46] in which there are an infinite number of vector mesons weakly coupled to the photon, the shadowing should gradually increase with energy. Instead, if the shadowing does not change with energy, a

direct electromagnetic interaction must exist, perhaps of the bare photon with constituents of the nucleon.[31] Indeed, it has been pointed out[47] that such a short-range interaction is a consequence of the existence of partons, or nucleon constituents. Independently of our earlier analysis,[11,48] Brodsky *et al.*[47] have shown that roughly 20% of the total photoabsorption cross section should result from the photon-parton interaction. By now it is perhaps surprising, not that we have observed a short-range interaction, but that the fraction of the cross section ascribable to such an interaction is not large enough to accommodate all of its possible sources.

ACKNOWLEDGMENTS

We wish to thank Bruce W. Worster and George E. Jahn for their assistance in carrying out the experiment and Burton N. Kendall for help in the analysis. Special thanks go to Donald R. Yennie for theoretical help and for the use of his optical model calculations. Earlier publications have already acknowledged the considerable aid received from many people at SLAC.

---

*Work supported in part by the U. S. Atomic Energy Commission.

†Presently a Guggenheim Fellow at CERN, Geneva, Switzerland.

‡Now at the Department of Physics and Astronomy, University of Hawaii, Honolulu, Hawaii 96822.

[1]D. O. Caldwell *et al.*, Phys. Rev. Letters 23, 1256 (1969); 24, 796(E) (1970).

[2]D. O. Caldwell *et al.*, Phys. Rev. Letters 25, 609 (1970); 25, 902(E) (1970); W. P. Hesse *et al.*, *ibid.* 25, 613 (1970); 25, 902(E) (1970); 25, 979(E) (1970); in *High Energy Physics and Nuclear Structure*, edited by S. Devons (Plenum, New York, 1970), p. 387.

[3]M. Ross and L. Stodolsky, Phys. Rev. 149, 1172 (1966).

[4]J. J. Sakurai, Ann. Phys. (N.Y.) 11, 1 (1960); M. Gell-Mann and F. Zachariasen, Phys. Rev. 124, 953 (1961); Y. Nambu and J. J. Sakurai, Phys. Rev. Letters 8, 79 (1962); M. Gell-Mann, D. Sharp, and W. G. Wagner, *ibid.* 8, 261 (1962); N. M. Kroll, T. D. Lee, and B. Zumino, Phys. Rev. 157, 1376 (1967); H. Joos, Acta Phys. Austr. Suppl. IV (1967).

[5]Here f is really f_1, the amplitude for parallel polarization vectors of the initial and final photons, but it is also the only amplitude remaining after averaging over nucleon spins. From a comparison of the data of this experiment with that from Compton scattering, as will be discussed later, it is found that the amplitude for perpendicular polarization vectors, f_2, is less than 10% of f_1.

[6]L. Stodolsky, Phys. Rev. Letters 18, 135 (1967).

[7]This distance can be obtained in another way, using a different but equivalent description of the process which has been emphasized by S. J. Brodsky and J. Pumplin, Phys. Rev. 182, 1794 (1969), and particularly V. N. Gribov, Zh. Eksp. Teor. Fiz. 57, 1065 (1969) [Sov. Phys. JETP 30, 709 (1970)]. If the photon virtually becomes a vector meson of mass m_V, then the meson travels a distance R limited according to the uncertainty principle by the energy change ΔE from E_γ to

$$(E_\gamma^2 + m_V^2)^{1/2} \approx E_\gamma + m_V^2/2E_\gamma,$$

so that

$$\Delta E \Delta t \approx (m_V^2/2E_\gamma)(R) \sim 1 \text{ for } c = \hbar = 1.$$

[8]K. Gottfried and D. Yennie, Phys. Rev. 182, 1595 (1969); D. Yennie, Lecture Notes from the Eleventh Scottish University Summer School in Physics, 1970 (unpublished). Parameters used include density functions for both copper and lead of

$$\rho(r) = \rho_0\{1 + \exp[(r-c)/a]\} - 1,$$

with $a = 0.545$ F, $c = 1.12A^{1/3}$ F, and for carbon,

$$\rho(r) = \rho_0[1 + \tfrac{4}{3}(r/a)^2]e^{-(r/a)^2},$$

with $a = 1.65$ F; charge-smearing parameters $RS = REM = 0.8$ F; $l_c = 0.3$ F; $\sigma(\omega N) = 25$ mb; $\sigma(\phi N) = 12$ mb; diffraction-peak slopes $b_\rho = b_\omega = 8$ (GeV/c)$^{-2}$, $b_\phi = 5$ (GeV/c)$^{-2}$; $4\pi/\gamma_\rho^2$: $4\pi/\gamma_\omega^2$: $4\pi/\gamma_\phi^2 = 9:1:2$; and $\eta_\omega = \eta_\phi = -0.2$.

[9]D. Yount, Nucl. Instr. Methods 52, 1 (1967); in Proceedings of the Symposium on Beam Intensity Measurement, Daresbury, England (Daresbury Nuclear Physics Laboratory Report No. DNPL/R1, 1968, p. 75) (unpublished).

[10]Trident production: Theory – T. Murota, A. Ueda, and H. Tanaka, Progr. Theoret. Phys. (Kyoto) 16, 482 (1956); P. Stähelin, DESY Lecture Notes, 1966 (unpublished); Experiment – B. Grossetête *et al.*, Phys. Rev. 168, 1475 (1968). A detailed calculation for our geometry is given in the following reference.

[11]W. P. Hesse, Ph.D. thesis, University of California at Santa Barbara, 1971 (unpublished).

[12]H. Nagel, Z. Physik 186, 319 (1965); U. Völkel, DESY Report No. 65/6, 1965 (unpublished). See also W. R. Nelson, T. M. Jenkins, R. C. McCall, and J. K. Cobb, Phys. Rev. 149, 201 (1966).

[13]R. J. Tapper, Rutherford High Energy Laboratory Report No. NIRL/R/95, 1965 (unpublished).

[14]J. H. Hubbell, National Bureau of Standards Report No. NSRDS-NBS-29, 1969 (unpublished).

[15]P. Joos, DESY-HERA Report No. 70-1, 1970 (unpublished); R. L. Anderson *et al.*, Phys. Rev. Letters 25, 1218 (1970); W. G. Jones *et al.*, *ibid.* 21, 586 (1968); H. G. Hilpert *et al.*, Nucl. Phys. B23, 45 (1970).

[16]A. M. Boyarski *et al.*, Phys. Rev. Letters 23, 1343 (1969); G. McClellan *et al.*, *ibid.* 22, 377 (1969); F. Bulos *et al.*, *ibid.* 22, 490 (1969).

[17]Brodsky and Pumplin (Ref. 7).

[18]V. Franco and R. Glauber, Phys. Rev. 142, 1195 (1966).

[19]B. Naroska, Ph.D. thesis (DESY Report No. DESY-F1-70/3, 1970) (unpublished); H. Meyer *et al.*, Phys. Let-

ters 33B, 189 (1970); H. Meyer *et al.*, in *Proceedings of the Fourth International Symposium on Electron and Photon Interactions at High Energies, Liverpool, 1969,* edited by D. W. Braben and R. E. Rand (Daresbury Nuclear Physics Laboratory, Daresbury, Lancashire, England, 1970); V. Heynen *et al.*, Phys. Letters 34B, 651 (1971).

[20]G. B. West, Phys. Letters 37B, 509 (1971); Ann. Phys. (N.Y.) (to be published); W. B. Atwood and G. B. West, Phys. Rev. D 7, 773 (1973).

[21]C. A. Dominguez, J. F. Gunion, and R. Suaya, Phys. Rev. D 6, 1404 (1972); see also Atwood and West (Ref. 20).

[22]T. A. Armstrong *et al.*, Phys. Rev. D 5, 1640 (1972) [$\sigma_T(\gamma p)$ from 0.265 to 4.215 GeV]; Nucl. Phys. B41, 445 (1972) [$\sigma_T(\gamma d)$ from 0.265 to 4.215 GeV].

[23]E. D. Bloom *et al.*, SLAC Report No. SLAC-PUB-653, 1969 (unpublished).

[24]M. Roos *et al.*, Phys. Letters 33B, 1 (1970).

[25]J. Ballam *et al.*, Phys. Rev. Letters 21, 1544 (1968) (7.5 GeV); 23, 498 (1969) (1.44, 2.8, and 4.7 GeV).

[26]To avoid congestion in the plot, only every fifth point of the Daresbury data is plotted.

[27]H. Harari, Phys. Rev. Letters 17, 1303 (1966).

[28]W. W. Wada, Phys. Letters 34B, 317 (1971).

[29]J. L. Rosner (private communication).

[30]G. C. Fox and D. Z. Freedman, Phys. Rev. 182, 1628 (1969).

[31]A. suri and D. R. Yennie, Ann. Phys. (N.Y.) 72, 243 (1972).

[32]I. Shibasaki, T. Minamikawa, and T. Watanabe, Progr. Theoret. Phys. (Kyoto) 46, 173 (1971).

[33]M. Damashek and F. Gilman, Phys. Rev. D 1, 1319 (1970).

[34]C. A. Dominguez, C. Ferro Fontan, and R. S. Suaya, Phys. Letters 31B, 365 (1970).

[35]M. J. Creutz, S. D. Drell, and E. A. Paschos, Phys. Rev. 178, 2300 (1969).

[36]G. Buschhorn *et al.*, Phys. Letters 33B, 241 (1970); R. Anderson *et al.*, Phys. Rev. D 1, 27 (1970); A. M. Boyarski *et al.*, Phys. Rev. Letters 26, 1600 (1971).

[37]D. Benaksas *et al.*, Phys. Letters 39B, 289 (1972).

[38]H. Blechschmidt *et al.*, Nuovo Cimento 52A, 1348 (1967); W. G. Jones *et al.*, Phys. Rev. Letters 21, 586 (1968); M. Davier *et al.*, *ibid.* 21, 841 (1968); R. Erbe *et al.*, Phys. Letters 27B, 54 (1968); G. McClellan *et al.*, Phys. Rev. Letters 22, 374 (1969); F. Bulos *et al.*, *ibid.* 22, 490 (1969); Y. Eisenberg *et al.*, *ibid.* 22, 669 (1969); H. Alvensleben *et al.*, *ibid.* 23, 1058 (1969); H. H. Bingham *et al.*, *ibid.* 24, 955 (1970); H. Ogren, Cornell University Report No. CLNS-154, 1971 (unpublished).

[39]Y. Eisenberg *et al.*, Nucl. Phys. B42, 349 (1972).

[40]G. McClellan *et al.*, Phys. Rev. Letters 22, 377 (1969); H. J. Behrend *et al.*, *ibid.* 24, 336 (1970); H. Alvensleben *et al.*, Nucl. Phys. B18, 333 (1970); R. L. Anderson *et al.*, Phys. Rev. D 4, 3245 (1971).

[41]E. J. Moniz and G. D. Nixon, Ann. Phys. (N.Y.) 67, 58 (1971).

[42]M. Davier *et al.*, in *Proceedings of the International Symposium on Photon and Electron Interactions at High Energies, 1971,* edited by N. B. Mistry (Cornell Univ. Press, Ithaca, N. Y., 1972); SLAC Report No. SLAC-PUB-666, 1972 (unpublished).

[43]G. Smadja *et al.*, in *Experimental Meson Spectroscopy–1972,* edited by Kwan-Wu Lai and A. H. Rosenfeld (A.I.P., New York, 1972).

[44]G. Barbarino *et al.*, Lett. Nuovo Cimento 3, 689 (1972); 4, 200(E) (1972); A. Bramon and M. Greco, *ibid.* 1, 739 (1971).

[45]A. Benvenuti *et al.*, Phys. Rev. Letters 27, 283 (1971).

[46]J. Cleymans and R. Rodenberg, Nuovo Cimento 5A, 297 (1971).

[47]S. J. Brodsky, F. E. Close, and J. F. Gunion, Phys. Rev. D 6, 177 (1972).

[48]D. O. Caldwell *et al.*, University of California at Santa Barbara report (unpublished). This work, first circulated in late 1971 and giving the experimental case for a short-range interaction, was never published, but it contained essentially the same conclusions as are presented here.